COMPACTION EFFECT ON DIFFERENT DENSITIES OF CANCELLOUS BONE AND IMMEDIATE STABILITY OF AN ANGLE STABLE INTERLOCKING NAIL IN A DISTAL FEMORAL OSTEOTOMY MODEL

By

Agnieszka Beata Fracka

A THESIS

Submitted to
Michigan State University
in partial fulfillment of the requirements
for the degree of

Comparative Medicine and Integrative Biology – Master of Science

2025

ABSTRACT

Background: Interlocking nails are becoming a common alternative to plates used to stabilize the femur following corrective surgery for medial patellar luxation. Intraoperative manipulation of the femoral condyle can lead to loss of initial nail stability, increasing the risk of malalignment. The use of cancellous bone compaction, as opposed to traditional reaming, has the potential to improve the mechanical properties of the nail-bone construct.

Objectives: To evaluate the effect of compaction on the microstructure and mechanical properties of the bone/nail interface in a simulated femoral condylar bone model.

Methods: Foam models of different densities (7.5, 10, 12.5, 15, and 20 PCF, n=5/group) were prepared using either standard line-to-line reaming (7 mm) or sequential compaction using custom mandrels of increasing diameters from 4 mm to 7 mm. Five samples from each group were tested in mediolateral bending. Impaction stiffness was assessed for each mandrel size and I-Loc nail in compacted foams (n=4/group). Three specimens per group were evaluated by micro-computed tomography (micro-CT) to define the effects of compaction on foam microstructure.

Results: Compaction increased both construct bending stiffness, as well as load at 5 mm displacement across all tested foam densities ($p<0.0001$). Impaction test showed increasing stiffness and load at 32 mm from 4 mm mandrel to 7 mm mandrel, with the I-Loc nail performing similarly to the 6 mm mandrel. Micro-CT scan results demonstrated that higher density foams (10 PCF and above) exhibited more pronounced differences between drilled and compacted samples. Compaction effects on microstructure were quantified, showing increased local density and altered pore morphology in compacted regions.

Conclusion: Compared to conventional reaming, cancellous bone compaction significantly increases the immediate stability of the bone/nail interface in a distal femoral osteotomy model.

This thesis is dedicated to my beloved parents, who have been my shining light in what often felt like a long and challenging tunnel.

Mamo i Tato z calego serca pragne Wam podziekować za to, że zawsze jesteście przy mnie. Jesteście moim najwiekszym źródłem inspiracji i bez Waszego wsparcia i pomocy nie osignęłabym tego, co mam dzisiaj. Wy zawsze byliście moim najjaśniejszym światłem w tunelu, dzięki któremu nigdy się nie zgubiłam. W chwilach zwątpienia i trudności to właśnie Wasza miłość i troska dawały mi siłę do dalszej nauki i pracy. Wasze mądre rady pozwoliły mi pokonywać wszelkie przeszkody i dążyć do wyznaczonych celów. Dziękuję, że jesteście nie tylko najlepszymi rodzicami jakich mogłabym sobie tylko wymarzyć, ale i moimi najlepszymi przyjaciółmi, którzy zawsze są gotowi mnie wysłuchać i wesprzeć w każdej sytuacji. Wasza bezwarunkowa miłość i oddanie są dla mnie największym skarbem i darem, za który jestem nieskończenie wdzięczna.

ACKNOWLEDGEMENTS

I am deeply grateful to my advisor, mentor, and friend, Loic Dejardin, whose unwavering belief in me, even in moments of self-doubt, has been a constant source of strength. His encouragement has driven me to strive for excellence, surpass my limits, and grow both professionally and personally. I greatly admire his knowledge and surgical skills and aspire to one day reach his level of expertise in my own work.

I would like to express my heartfelt gratitude to my dear friend and mentor, Matthew Allen, whose unwavering support has been a cornerstone of my journey. His belief in my potential and his willingness to help in every way mean the world to me. Whether offering academic insight, emotional support or sharing in challenges and triumphs, he has been a true inspiration. The countless hours of discussion, guidance, and shared passion for our field have been pivotal in my professional growth.

My sincere thanks go to the Physics (Machine Shop) team, particularly Rob, Mike and Tom for their invaluable contribution in fabricating the fixtures essential for my thesis experiments. Their expertise made our testing possible.

I also would like to extend my appreciation to Maria Podsiedlik for her assistance in data collection during mechanical testing for this project. Additionally, I am thankful to both Michael Lavagnino and Maria Podsiedlik for serving as members of my MS committee.

TABLE OF CONTENTS

LIST OF ABBREVIATIONS

aLDFA– Anatomic lateral distal femoral angle

AMI – Area moment of inertia

AS-ILN – Angle stable interlocking nail

CORA – Center of rotation of angulation

DFO – Distal femoral osteotomy

DFV – Distal femoral varus

FVA – Femoral varus angle

ILN – Interlocking nails

IMRs – Intramedullary rods

MIO – Minimally invasive osteosynthesis

Micro-CT – Micro-computed tomography

MPL – Medial patellar luxation

NS – Not significant

PCF – Pounds per cubic foot

PU – Polyurethane

SD – Standard deviation

INTRODUCTION

Medial patellar luxation (MPL) is a frequently encountered orthopedic disease affecting the stifle joint in dogs that commonly causes pelvic limb lameness (1). Despite its prevalence, the precise cause of this disorder has yet to be fully determined (2,3). However, it is suspected that a decreased angle between the femoral neck and femoral shaft (coxa vara) as well as a reduced angle between the femoral neck and the caudal condylar joint line (femoral anteversion) may play a significant role in MPL. These abnormalities contribute to displacement of the quadriceps muscle, which pulls the patella out of the trochlear groove. Additionally, other recognized risk factors for MPL include angular pelvic limb deformities such as distal femoral varus, external femoral torsion, internal tibial rotation; shallow trochlear groove, and tibial tuberosity displacement (1-4). These factors should be taken into consideration during the treatment of MPL to ensure adequate alignment of the quadriceps mechanism and therefore optimal clinical outcomes.

Standard surgical techniques for correcting patellar luxation typically include soft tissue releases or imbrication, tibial tuberosity transposition and deepening the trochlear groove (5). Although these procedures can effectively improve the quadriceps muscle alignment, they do not address femoral deformities, and failure to correct them may result in the recurrence of MPL and poor outcomes in certain cases (6).

The role and significance of the DFV in the development of medial patellar luxation is increasingly recognized and has been emphasized in recent research (6-9). It has been suggested that inadequate correction of femoral varus may contribute to the postoperative recurrence of MPL. As a result, the current approach of treating MPL has focused on addressing excessive femoral varus through corrective femoral osteotomies (8-10).

Most canine femora naturally have a mild varus typically from 4° to 8° with variations observed both within and across breeds (11). Physiologic distal femoral varus is quantified through measurement of the anatomic lateral distal femoral angle (aLDFA), estimated to be between 94-98° in normal dogs (11). The femoral varus angle (FVA) is defined as the angle formed between the anatomical axis of the femur in the frontal plane and a line that is perpendicular to the distal femoral joint line. Femoral correction is recommended in large breed dogs with FVA of more than 10°-12°, or an aLDFA of ≥ 102° (6,9). However, the effect of femoral varus deformities on MPL has not been critically evaluated. Moreover, the cutoff for surgically correcting aLDFA with a distal femoral osteotomy (DFO) remains controversial, despite anecdotal recommendations (12,13).

Angular limb deformity corrections particularly these involving distal femur are often performed using a combination of lateral closing wedge ostectomies and plate fixation (14). However, it is recommended that the ostectomy is performed at the center of rotation of angulation (CORA), which represents the point of maximal deformity (15). In some cases, this point may be situated quite distally on the femur. This approach presents significant challenges, especially when the apex of the deformity is located in the epi-metaphyseal region, as is often seen in distal femoral varus (DFV) with secondary MPL. These procedures typically require an extensive approach to accommodate a jig that maintains fragments alignment until plate fixation is completed. Other limitations include the paucity of appropriate plate sizes, limited bone stock available for screw anchorage, which can jeopardize the stability of the construct and increase the risk of implant failure via screw pullout, or the presence of a transcortical gap. Additional challenges include screw interference with adjacent structures such as femoral trochlea, loss of primary reduction and alignment due to non-anatomical plate contouring, which may lead to medial patellar luxation

recurrence, and technical challenges associated with closing, often biplanar ostectomies that require perfect cortical apposition to prevent implant fatigue failure (15-17). Given these limitations and challenges, it is perhaps not surprising that complication rates of up to 12% have been reported following DFV correction with closing wedge ostectomies and lateral plate fixation for the treatment of MPL (12).

Interlocking nails (ILN) have been shown to be an excellent alternative to plate fixation (17). Despite the differences in the ILN designs, they share several features. They are robust intramedullary rods (IMRs) with cannulations at both ends or along their entire length (Durall system). Original veterinary nails, often referenced as "standard nails" are secured using screws or partially threaded bolts that penetrate both cortices of the bone and the nail itself. At the proximal end, the nail incorporates keying flanges, allowing for a firm connection to an alignment guide. The distal tip of the nail is rounded or trocar-shaped to assist with insertion (17). Nails come in a range of diameters (4 – 10 mm) and lengths (68 – 230 mm) to fit dogs and cats of various sizes. Each nail end has 1 or 2 smooth channels designed to hold bolts or locking screws of different sizes (2.0 – 4.5 mm). To enhance the device's adaptability, especially for treating fractures near joints, these channels are spaced either 11 or 22 mm apart. Closer spacing is better for fractures near joints, where limited bone stock is available for inserting two interlocking bolts (17).

Interlocking nails are considered the gold standard for long bone fracture repair in human medicine. To fully appreciate the efficacy of ILNs, it is essential to understand the biomechanical principles behind their design and placement. The success of ILNs lies in their precise positioning within the bone. Like other intramedullary devices, ILNs are inserted near the bone's neutral axis, a location that protects the implant from the detrimental effect of cycling bending. This is

significant, because of the forces acting on bones during normal physiological activities. These forces cause compressive and tensile load on opposite sides, generating bending moments along their length. The neutral axis refers to a theory where these forces along with associated bending moments are neutralized and balance each other out (18). This concept is crucial in ILN placement. When an ILN is positioned closer to this neutral axis, it experiences less stress from bending forces. Conversely, implants located farther from the neutral axis, e.g. bone plates, are subjected to greater bending stresses, increasing their vulnerability to fatigue failure over time due to repeated loading cycles (19,20). This principle highlights one of the primary advantages of ILNs in fracture repair and distal femoral osteotomy fixation.

While the precise location of a neutral axis is unclear, it is generally believed to be either near or within the medullary cavity. This positioning gives ILN a mechanical advantage over bone plates or external fixators, especially in procedures like minimally invasive osteosynthesis (MIO), where precise anatomic reconstruction is not required. Moreover, ILNs are typically made from stainless steel (21,22) and feature larger area moment of inertia (AMI) than size-matched bone plates (23,24). These characteristics contribute to their exceptional resistance to bending. The AMI describes material distribution relative to the deformation plane or axis and determines the implant's bending and torsional stiffness. For ILNs, it has been shown that the AMI is proportional to the fourth power of the nail's diameter, whereas for plates it scales with the cube of their thickness (17). As a result, while a plate's AMI can vary significantly depending on its orientation, the AMI of an ILN remains constant regardless of the load direction.

The popularity of ILNs relates to both biomechanical and biological advantages, including stability, an intramedullary location that facilitates trochlear realignment, low infection rates, and preservation of blood supply (25). Fractures may significantly compromise intramedullary blood

supply, making extra-osseous circulation vital for bone healing. Interlocking nails can be inserted through small incisions away from the fracture site preserving surrounding soft tissues and maintaining the extra-osseous blood flow (26,27). Furthermore, ILNs can be inserted in a normograde manner to minimize disturbance of the fracture area. This minimally invasive method reduces postoperative complications and enhances both fracture healing and functional outcomes.

Recently developed angle-Stable interlocking nails (AS-ILN) incorporate several design improvements compared to traditional ILNs. The first such nail, the I-Loc AS-ILN (Biomedtrix/Movora, Whippany, NJ) was developed with three key goals: enhancing structural stability, simplifying surgical procedure, and aligning with minimally invasive osteosynthesis (MIO) principles. Unlike standard nails, this angle stable and adaptable implant has main differences that lie in the unique locking system, modified shape, and the method of implantation (17). Its distinctive hourglass shape minimizes damage to the inner bone surface and blood supply while enhancing construct compliance (17). The nail's slender core diameter allows for easier insertion and generally eliminates the need for medullary cavity reaming. The nail's conical threaded cannulations, paired with corresponding central bolt section, use special asymmetric flanges at the proximal end to ensure adequate positioning and allow for a secure connection to an alignment guide. The nail also features an elongated, bullet-shaped tip that helps restore normal bone length during fracture repair, while reducing the chance of joint penetration (17).

The design of the I-Loc locking system has been associated with improved torsional and bending stiffness. Given the negative impact of acute deformation on bone healing, an AS-ILN may provide a more mechanically efficient repair method for diaphyseal and metaphyseal fractures compared to traditional ILNs (21,28,29). Additionally, AS-ILNs have proven effective in minimal interfragmentary movement and elimination of nail toggling, commonly referred to as "slack" that

led to a loss of post-operative reduction and alignment (30-32). From a biological perspective, the AS-ILN appears to enhance bone healing, leading to a faster recovery and formation of a stronger bone callus (33). These advantages have been shown to be effective in the treatment of unreconstructed metaphyseal fractures or osteotomies allowing surgeons to perform simpler opening wedge osteotomies rather than complex cuneiform osteotomies since perfect fragment apposition is no longer required (29,34). Such an AS-ILN, the I-Loc, has been developed for veterinary use and has become mainstream for fracture repair and distal angular deformities by virtue of its reduced rigidity (leading to lower risks of stress shielding), ease and accuracy of implantation, and excellent overall stability.

Distal femoral varus has been shown to be increasingly associated with medial patellar luxation in midsize and large canine breeds (8). Angular correction using the I-Loc AS-ILN offers additional multiple advantages such as a minimally invasive approach, less challenging procedure, lower risk of implant failure, and elimination of bone failure via screw pullout. Furthermore, the osteotomy site can be performed away from the deformity apex without inducing lateral displacement of the distal femoral segment (35). This is of particular interest since the apex of most DFV is located near the femoral trochlea which considerably limits the efficacy or even the feasibility of plate fixation. Additionally, an osteotomy performed proximal to the center of CORA can accommodate distal bolts.

Despite the established benefits of angle-stable locking nails, effective correction of MPL and DFV requires stability at the bone-implant interface during nail insertion. Current techniques for reaming the distal cancellous bone tunnel may fail to provide adequate bone-nail interface stability prior to locking. Subsequent loss of intraoperative alignment may lead to incomplete varus correction and patellar re-luxation. While initial implant stability is critical to appropriate bone

healing and construct integrity (36,37) it can be challenging to achieve in cancellous bone. Compaction drilling is a technique that relies on a series of drills or mandrels of increasing sizes to densify cancellous bone prior to screw insertion. While this technique has been shown clinically and experimentally to improve the initial stability of the cancellous bone-implant interface in human orthopedics (38,39) its potential benefits on immediate stability of the bone-nail interface has yet to be evaluated in the context of DFV correction.

Therefore, our study aims to determine the effect of compaction on different densities of cancellous bone and the immediate, pre-locking stability of the bone-nail interface in a distal femoral osteotomy model. We hypothesized that, compared to conventional drilling, cancellous bone compaction will increase bending stiffness, the load required to displace the nail by 5 mm, and the peak load sustained by the bone-nail construct. Clinically, this would result in significantly stronger bone-nail interface stability across all bone densities.

MATERIALS AND METHODS

Specimen preparation

To simulate the cortical bone of an osteotomized femoral condyle, 40 mm long custom-made aluminum hollow tubes (Figure 1) with a 20 mm outer diameter and a 2 mm wall thickness were used.

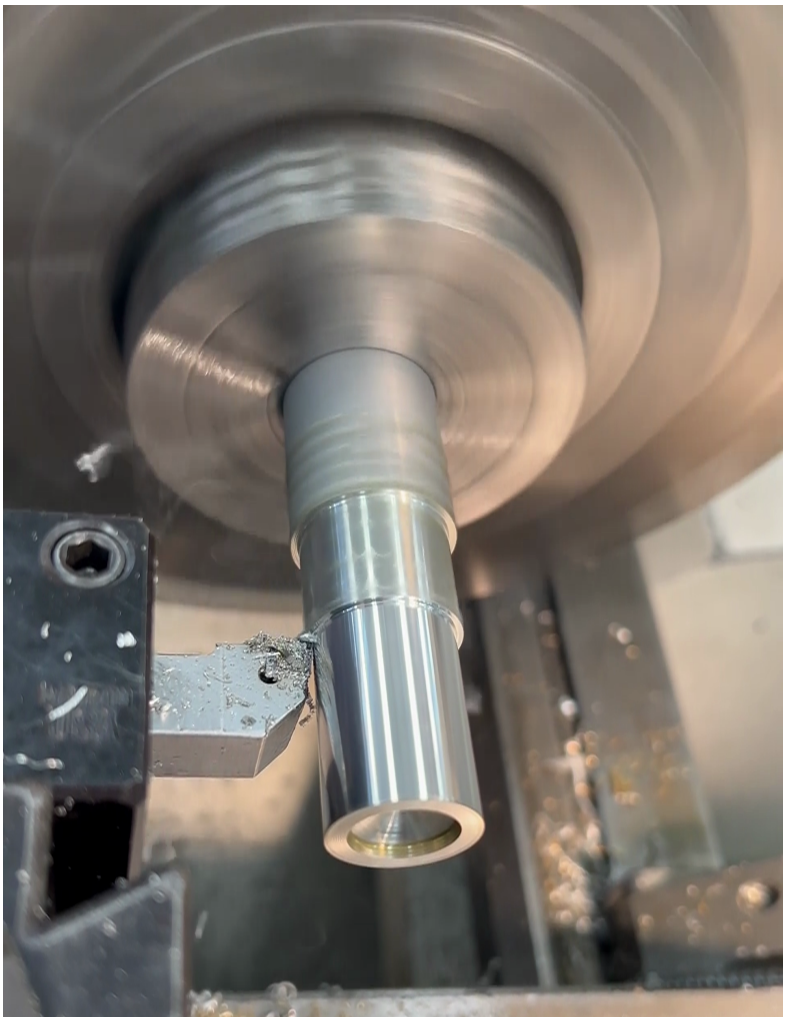

Figure 1: Machining process of a custom aluminum tube. The cutting tool is shaping the outer surface of the tube. These tubes were used for mechanical testing.

To simulate the cancellous bone of the distal femoral condyle, the tubes were filled with machined cylinders of 7.5 10, 12.5, 15, and 20 pounds per cubic foot (PCF) custom polyurethane (PU) foam (Sawbones USA; Vashon, WA) (Figure 2).

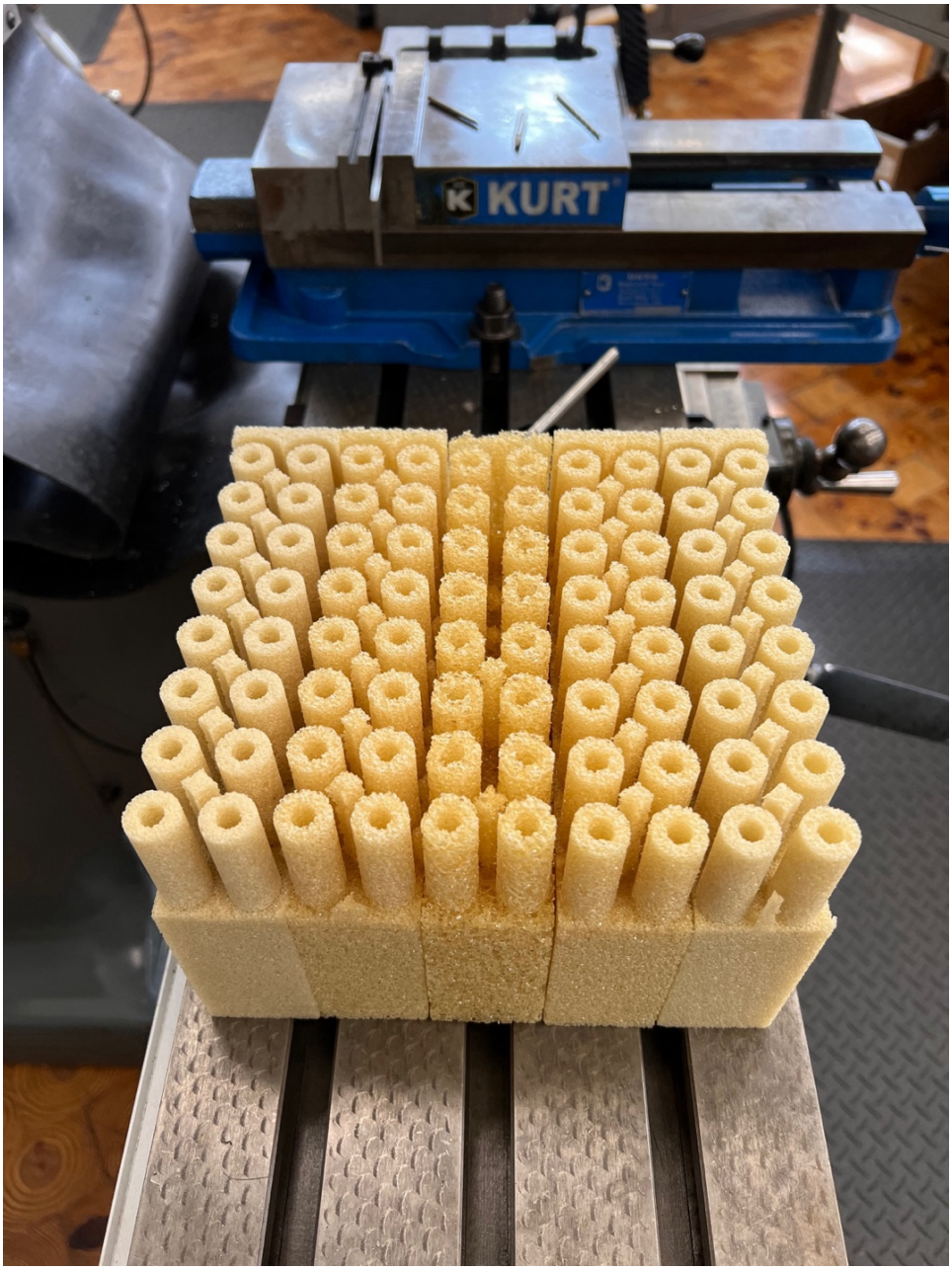

Figure 2: Different densities of the polyurethane (PU) foams. From outside to inside, these are 15 PCF, then 12.5 PCF, then 10 PCF. Foam specimens were machined in the Physics Department at Michigan State University.

The 12.5 and 15 PCF foam density/porosity have been shown to simulate normal cancellous bone (between osteoporotic and sclerotic bone) and have been used in numerous mechanical studies (40-42), while 10 PCF foam density mimics osteoporotic bone (43) and 20 PCF is more representative of dense (sclerotic) bone. When fully assembled, the model (Figure 3) simulates the distal femur of a medium-sized dog.

Figure 3: Synthetic bone model setup. Bottom of the picture: The synthetic bone model (right) is composed of a custom-made hollow aluminum tube (left) and a foam cylinder with a specified density of either 7.5, 10, 12.5, 15 or 20 PCF. Top of the picture: a custom-made horizontal fixture for the mediolateral bending test.

Each femoral condyle model was implanted with a 7 mm x160 mm I-Loc AS-ILN. Consistent with the current surgical technique, the I-Loc was centrally inserted into a drilled 7 mm line-to-line 40 mm deep pilot hole (DRILLED group). Alternatively, the nail was impacted into a sequentially compacted 40 mm deep defect that was prepared using custom mandrels of increasing diameters from 4 mm to 7 mm (COMPACTED group). All nails extended 30 mm into the drilled or compacted foam tunnel.

Pilot hole preparation

Drilling

The synthetic bone models were centered under a drill press using a custom loading cup. A central 6 mm pilot hole was drilled in the foam block to a depth of 40 mm (Figure 4).

A modified 7 mm I-Loc reamer was then loaded in the drill press and used to enlarge the pilot hole to its final dimension (7 mm x 40 mm). This technique created a drilled hole with the same dimensions as those of the nail by removing rather than compacting cancellous bone.

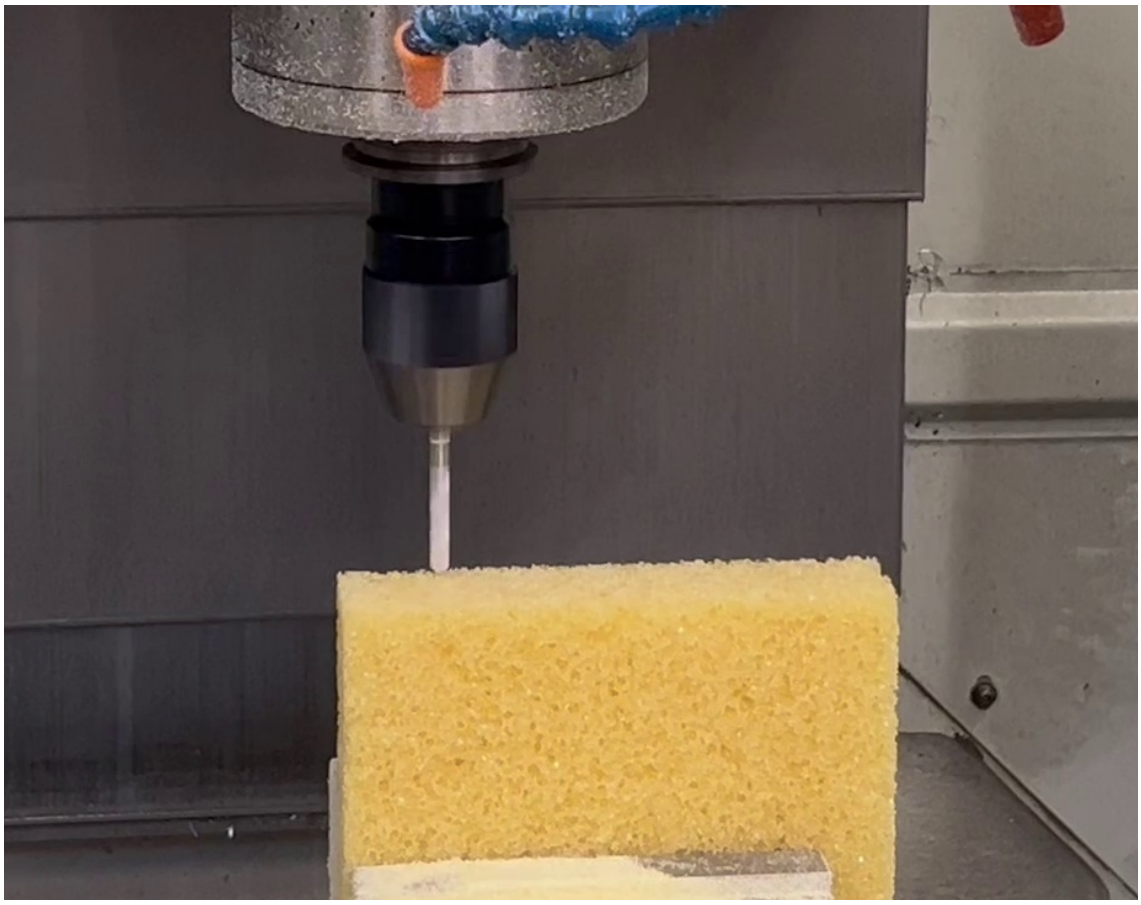

Figure 4: Drilling process of the foam block using a 6 mm drill bit. A 6 mm diameter drill bit is shown drilling into a 10 PCF foam block. The drill bit is mounted on a vertical CNC (computer numerical control) machining setup, with the foam block securely positioned beneath the drill.

Compaction

Synthetic bone models with a pre-drilled pilot hole of 3 mm (Figure 5) were positioned in the above-mentioned loading fixture and centered immediately below the compaction press to which a series of custom mandrels of increasing diameters (4 mm to 7 mm) were then attached (Figure 6).

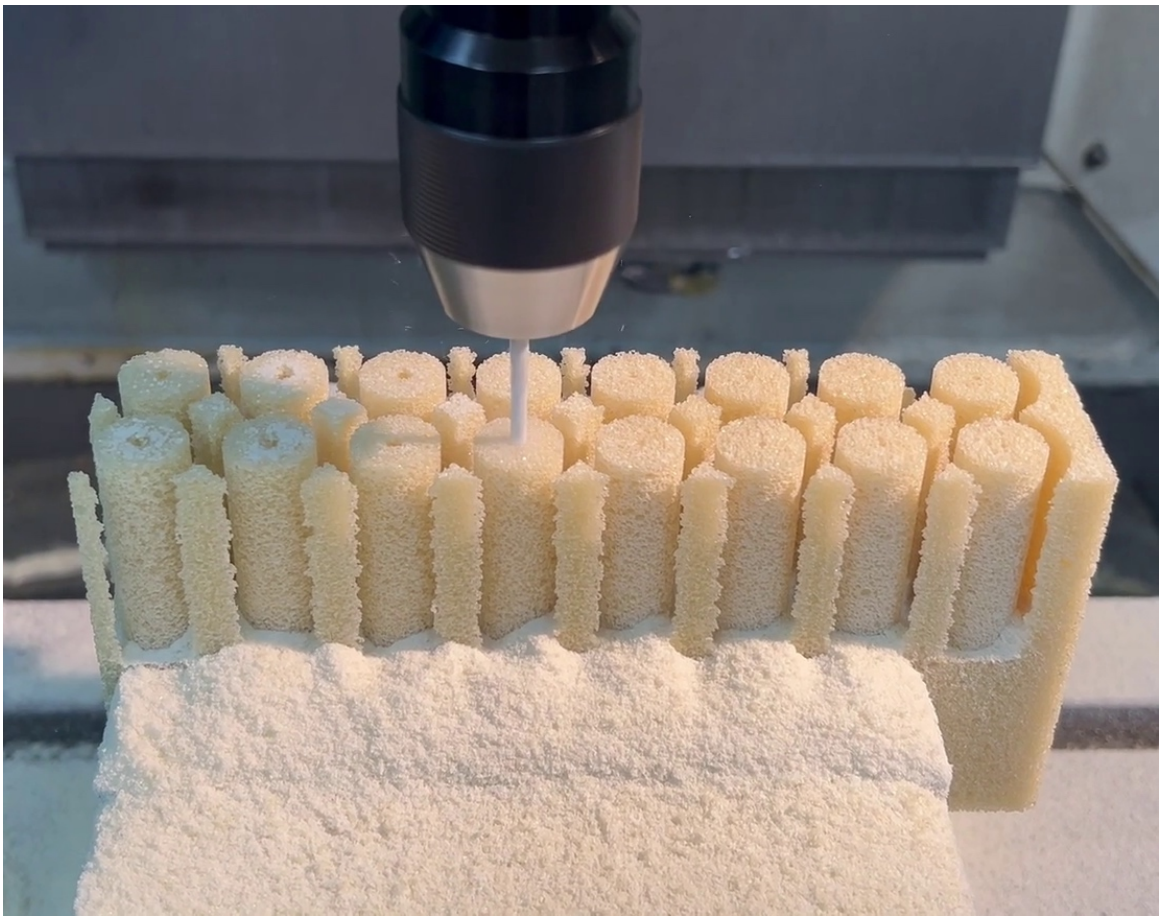

Figure 5: Drilling process of the foam specimens using a 3 mm drill bit. 15 PCF PU foam cylinders undergo precision drilling with a 3 mm diameter drill bit. The automated process creates consistent, uniform holes of the same size across multiple foam cylinders that were cut from a single foam block.

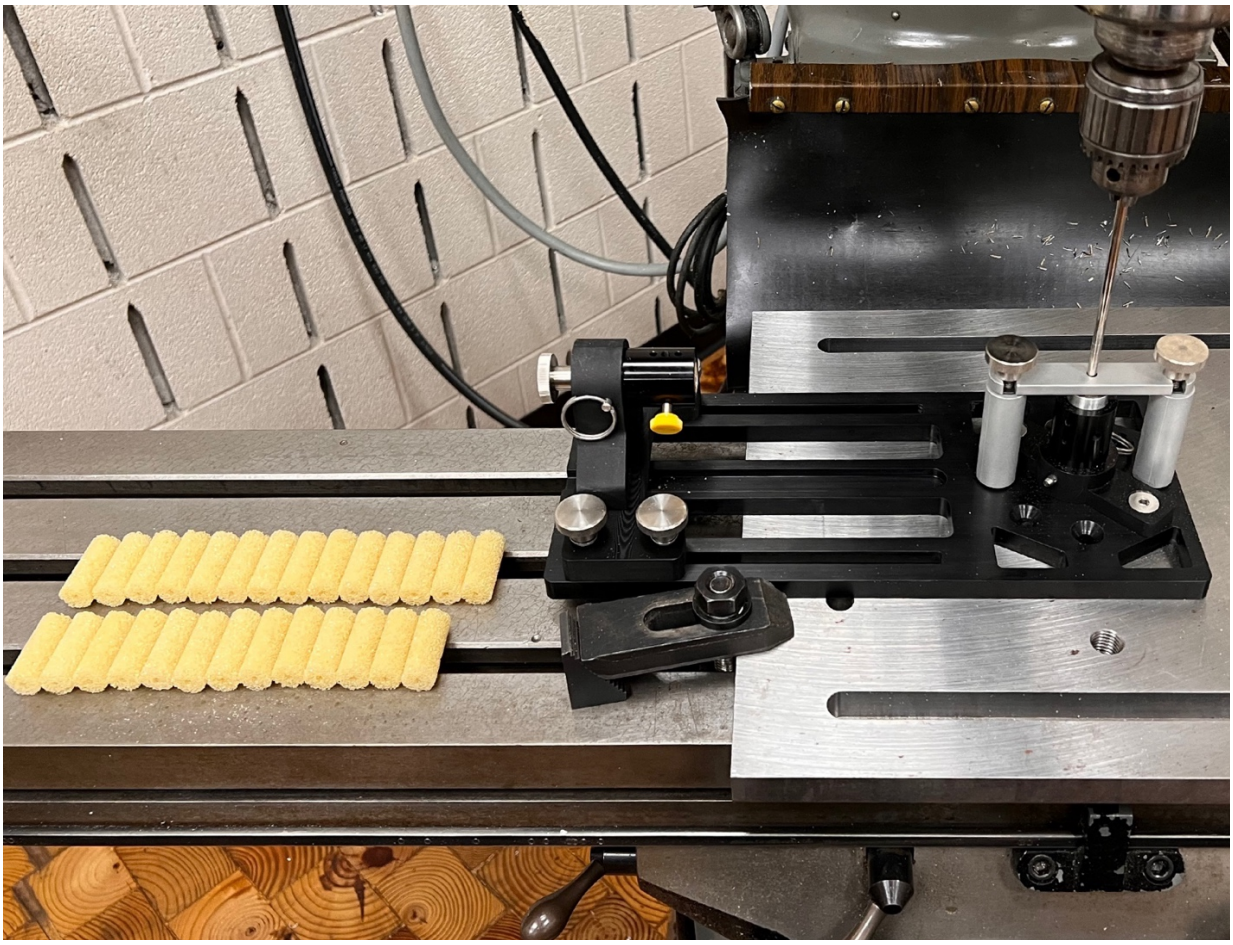

Figure 6: Mandrel mounted on compaction press machine in the process of foam compaction. A 7 mm mandrel is coupled to a vertical press (right) during compaction of the 12.5 PCF foam. A series of 12.5 PCF foam cylinders (left), previously compressed with 6 mm mandrel, ready for 7 mm mandrel compaction.

Each mandrel was impacted centrally to a depth of 40 mm and the resistance to impaction was determined (see below). This procedure gradually compacted the PU foam along the wall of the pilot hole, creating a peripheral ring of higher density adjacent to the central cavity in the foam. A centering bar was used to ensure the mandrels remained precisely positioned in the center of the pre-drilled pilot hole (Figure 7).

Figure 7: Image showing a centering bar. A centering bar is bolted to a base plate and positioned over an aluminum tube containing PU foam. The bar is attached to the base plate of the Instron with bolts and screws to ensure a secure position during the compaction process. The central hole in the bar helps guide the mandrel to the center of the foam. Mandrels of different sizes along with their corresponding centering bars are shown on the right.

Nail insertion

To prevent deformation of the pilot hole walls, a 7 mm 160 mm I-Loc nail was centrally inserted into the synthetic femoral bone model. The distal end of the nail extended 30 mm into the drilled or compacted foam tunnel.

Construct and fixtures

Two mechanical testing setups were used in this study. For the mediolateral bending test, bone model/I-Loc nail constructs (n=5/group) were mounted horizontally in a custom bending fixture secured to an Instron servo-hydraulic materials testing machine (Instron model 8501M/8800, Instron Corp, Canton, MA, USA). The proximal end of the nail was coupled to the Instron actuator via a U-joint (Figure 8).

A custom spacer was placed in the base plate recess to standardize the distance between the bending fixture and the I-Loc nail, to ensure consistent 30 mm nail insertion depth of the nail into the bone model during testing (Figure 8).

The second test setup was designed to evaluate the resistance of the foam specimens to sequential impaction by mandrels of different sizes. New synthetic bone models (n=4/each mandrel size) with a pre-drilled pilot hole of 3 mm were positioned in a dedicated loading cup and aligned with the central axis of the Instron actuator. The Instron actuator was fitted with a sequence of custom-made mandrels of increasing diameters from 4 mm to 7 mm and then an I-Loc nail (Figure 9).

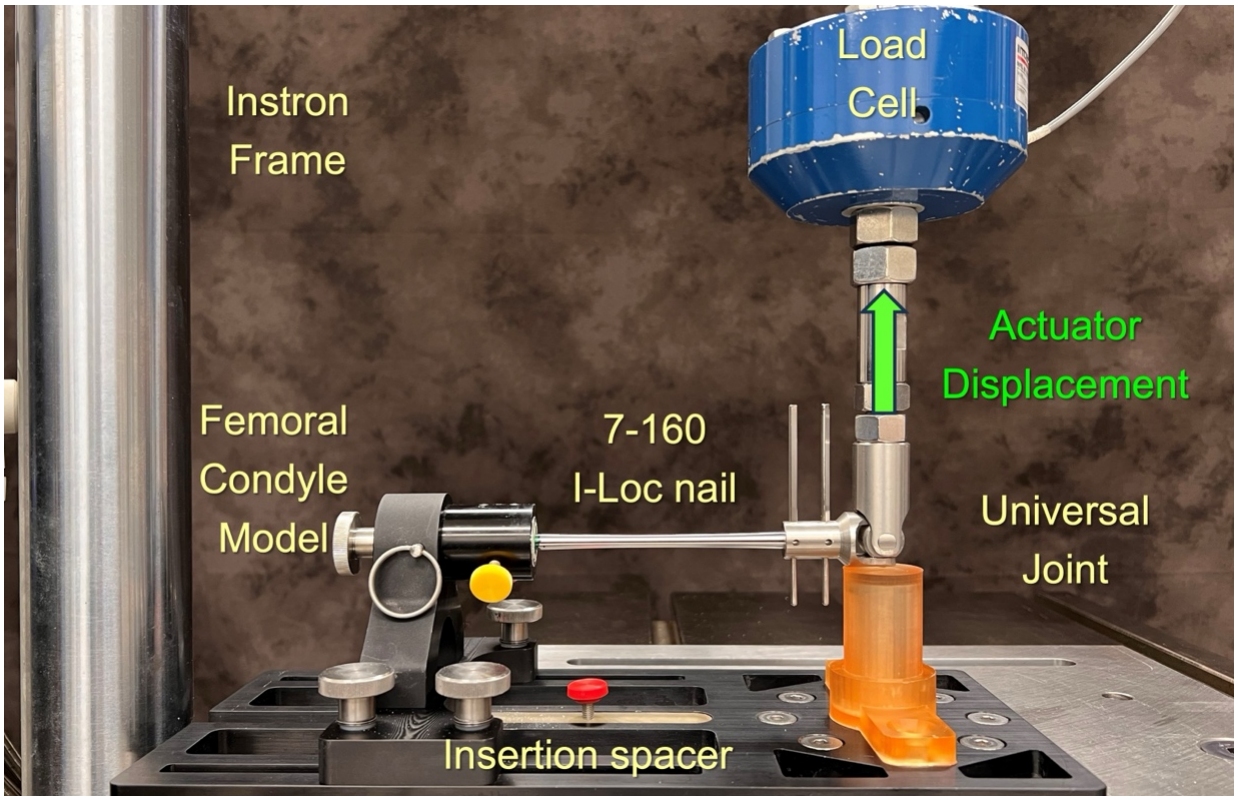

Figure 8: Mediolateral bending test setup. A custom-made bending fixture is secured to the base plate. An Instron load cell with a universal U-joint is shown with the I-Loc nail connected to the U-joint with locking bolts at one end (right) and inserted into the foam at the other (left). The green arrow indicates the testing direction. A spacer, represented by a light-yellow bar with a red screw head, was used to maintain the same nail insertion depth in all specimens.

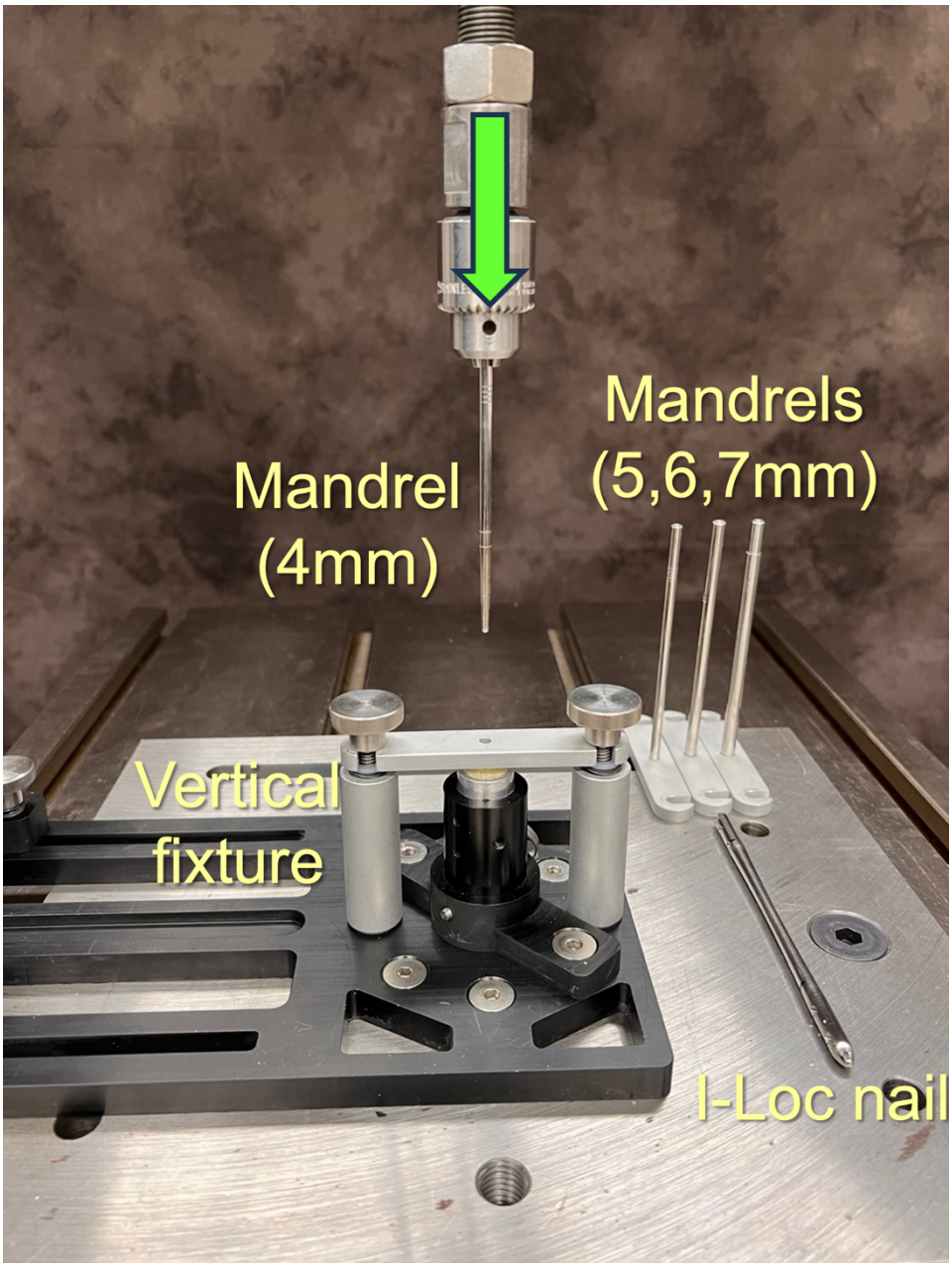

Figure 9: Impaction stiffness test setup. A vertical custom-made fixture is secured to the base plate and contains an aluminum tube filled with PU foam. A centering bar is placed on top of the aluminum tube. Above it, one of the mandrels (4 mm) is connected to the load cell of the Instron machine. The green arrow indicates the testing direction.

The horizontal bar placed over the loading cup ensured precise, central insertion of the mandrel or I-Loc nail into the foam. It also served to keep the foam securely in place, preventing it from being pushed out of the loading cup during testing.

Mechanical testing

Non-destructive bending (all groups)

Each construct underwent mechanical testing using an Instron materials testing machine. The Instron actuator was secured to a 2.225 kN linear load cell (Model 1010AF-500, Interface, Scottsdale, AZ, USA). Under displacement control, constructs were subjected to a single ramp load at a rate of 5 mm/sec. This protocol generated a mediolateral bending moment about the embedded nail. Maximum displacement was 19.5 mm, equivalent to a 7° change in nail angle relative to the original insertion axis (Figure 10).

Figure 10: Mediolateral bending test demonstrating 19.5 mm (7°) displacement of the I-Loc nail.

Impaction stiffness (compaction group only)

The mandrels and I-Loc nail were impacted into the foam blocks under displacement control at a rate of 5 mm/second, reaching a consistent depth of 35 mm (Figure 11).

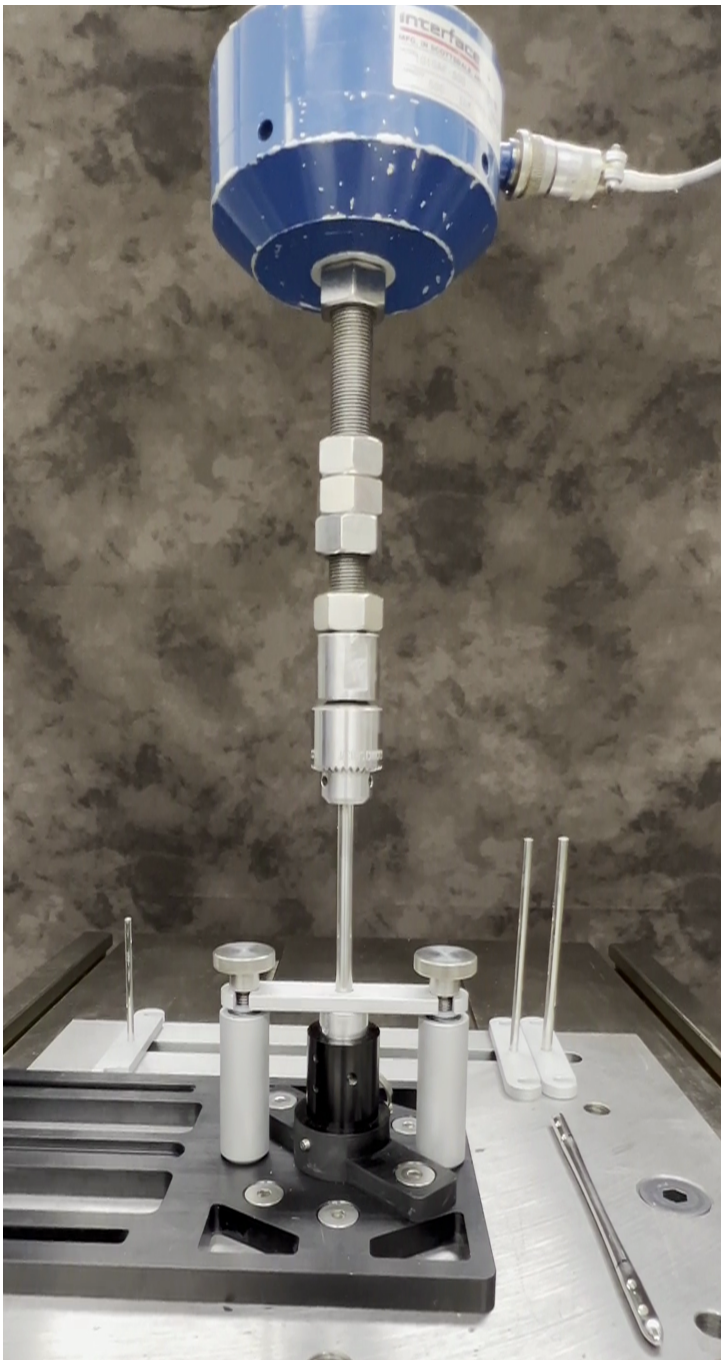

Figure 11: Impaction stiffness test. A mandrel is inserted into the PU foam through a centering bar, reaching a depth of 35 mm. The last compaction test was performed using a 7 mm I-Loc nail (right).

Force and displacement were monitored in real time and the initial stiffness (N/mm) was calculated and used as a measure of resistance to axial displacement.

Micro-computed tomography

To assess the effects of compaction on foam microstructure, a surrogate for cancellous bone microstructure, drilled and compacted foam specimens (n=3/group) of different densities (Figures 12-14) were evaluated by micro-computed tomography using an industrial micro-CT scanner (Nikon X-Tek H225 ST; Nikon X-Tek Systems Ltd., Tring, UK) operating at 85kV and 100 microamps, with a pixel size set at 30 micrometers. The foam microstructure of central cross sections was evaluated and Tagged Image File Format (TIFF) files were generated The TIFF images (Figures 15A and 16A) were imported into ImageJ (44) and global thresholding was used to highlight (in red) the area of foam material in the cross sections. Three circular regions of interest (ROIs) were then applied to the images (Figures 15B and 16B). The outer ROI (green circle) had a diameter of 20 mm and encompassed the entire foam specimen. The inner ROI (white circle) had a diameter of 7 mm and encompassed the central cavity created by drilling or compacting the specimen. The intermediate ROI (yellow circle) had a diameter of 12 mm and encompassed the central cavity plus a 2.5 mm wide circumferential zone of foam that had been either compacted (COMPACTED specimens) or not (DRILLED specimens). The total area of foam within the ROI was defined by adjusting the thresholding until all of the visible foam turned red (Figures 15C and 16C) and the total area of each ROI was calculated automatically by setting the threshold to detect all pixels in the field (Figures 15D and 16D).

Foam area fractions (in percentages) were calculated in two zones of interest – a peripheral, **non-compacted zone**, which occupied the area defined by subtracting the intermediate ROI from the outer ROI, and the **compacted zone**, which was defined by subtracting the inner ROI from the

intermediate ROI. After subtracting these data, the area fraction of foam in each zone was calculated by dividing the thresholded area (pixels^2) of foam within that zone by the total area (pixels^2) of the zone.

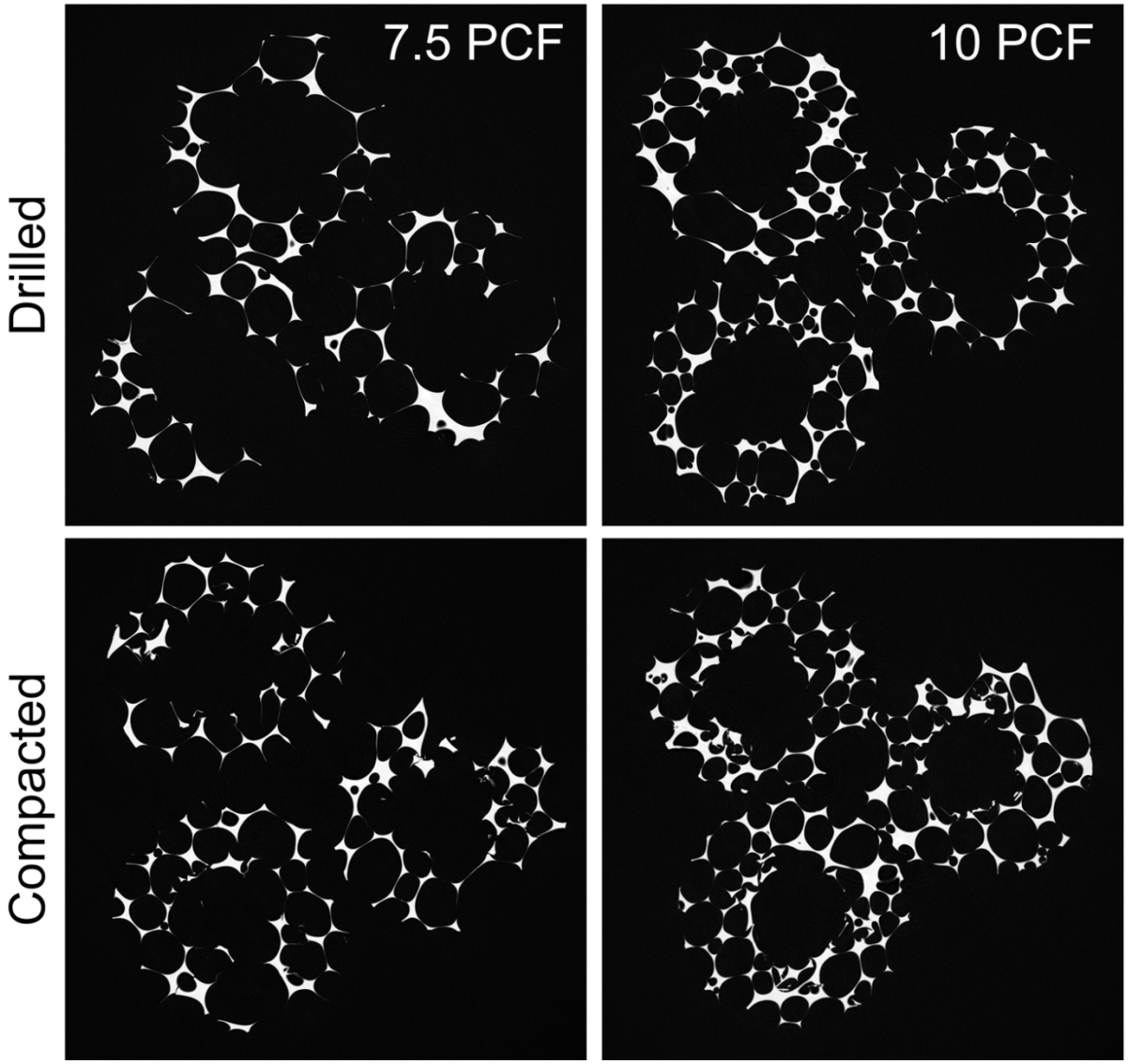

Figure 12: Micro-CT images with a set of three drilled (upper row) and compacted (lower row) 7.5 and 10 PCF foams.

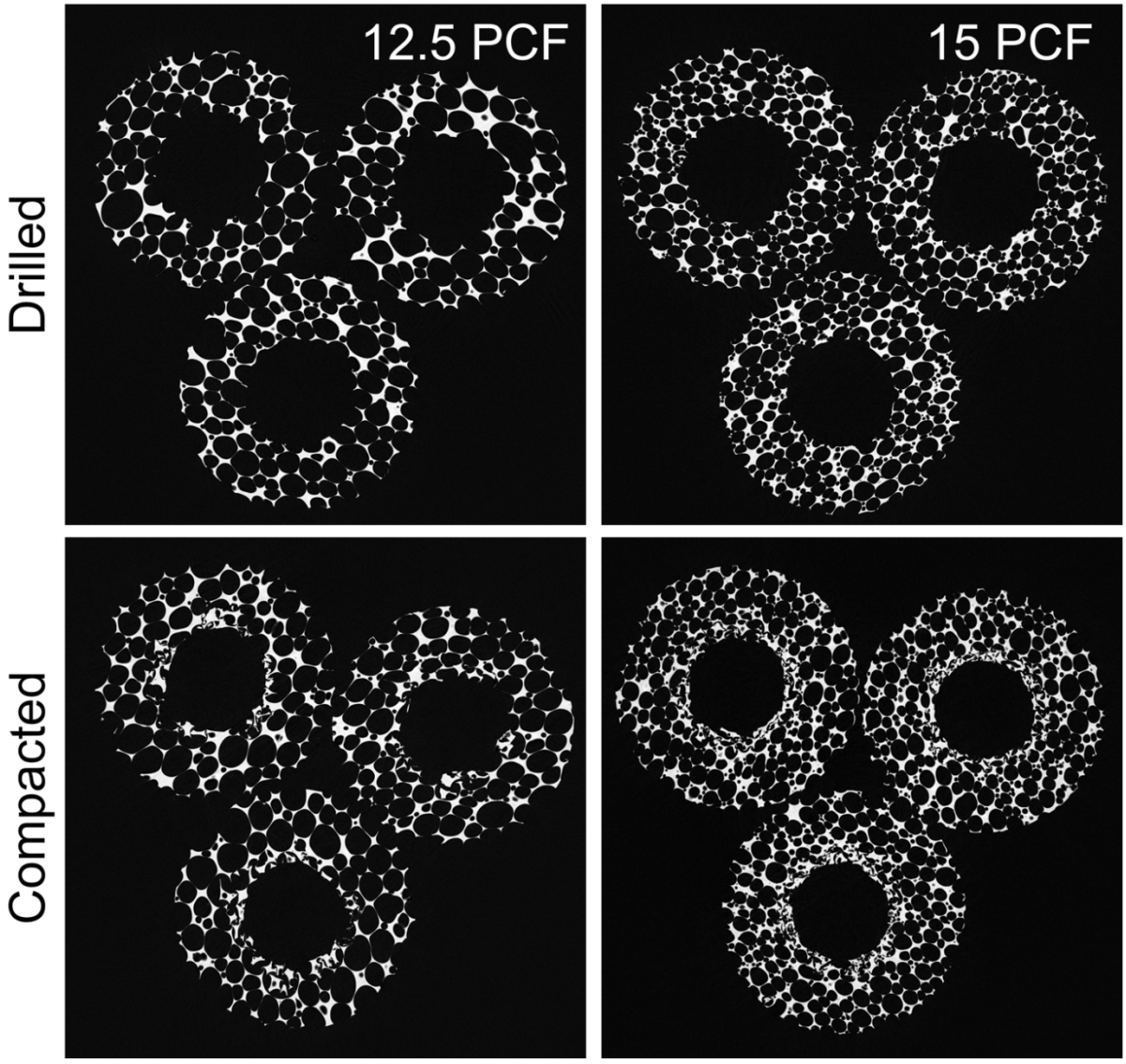

Figure 13: Micro-CT images with a set of three drilled (upper row) and compacted (lower row) 12.5 and 15 PCF foams.

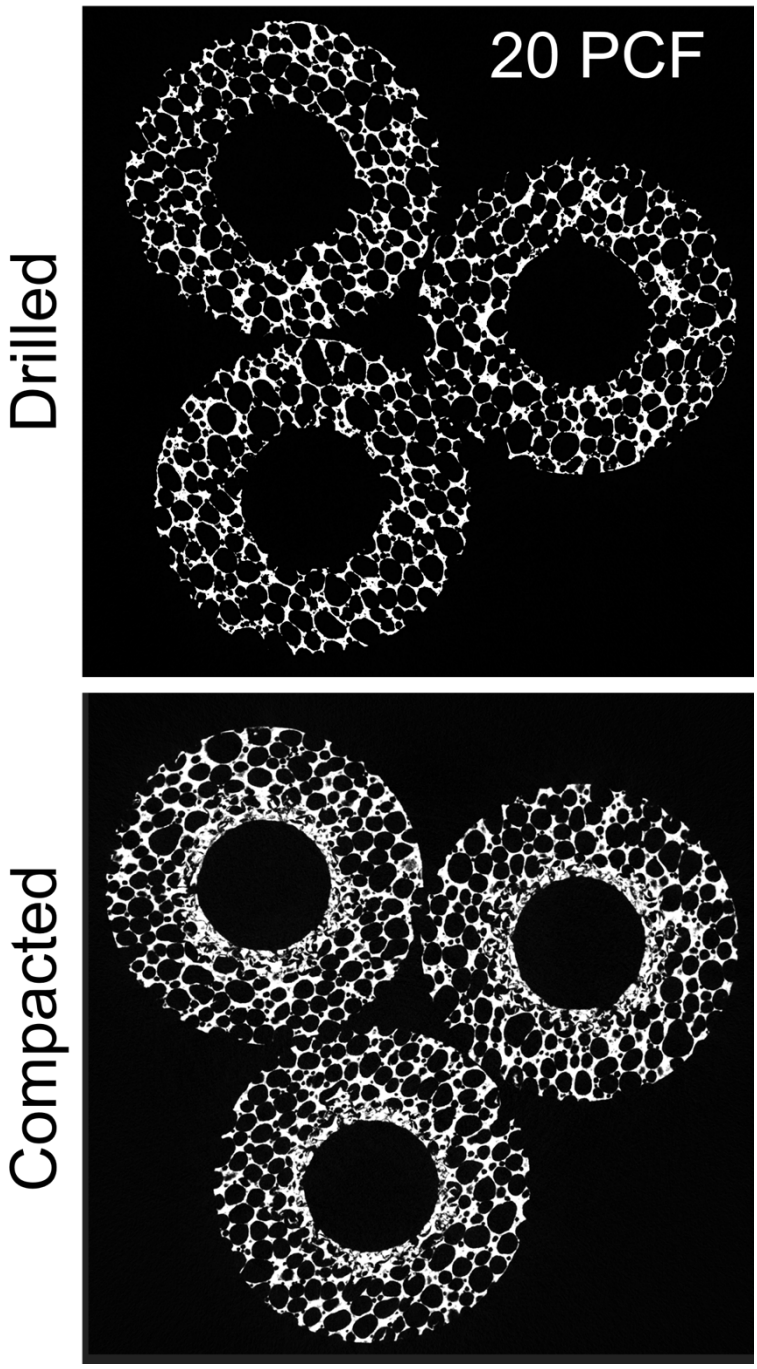

Figure 14: Micro-CT images showing sets of three foams, with 20 PCF drilled foams (top image) and compacted foams (lower image).

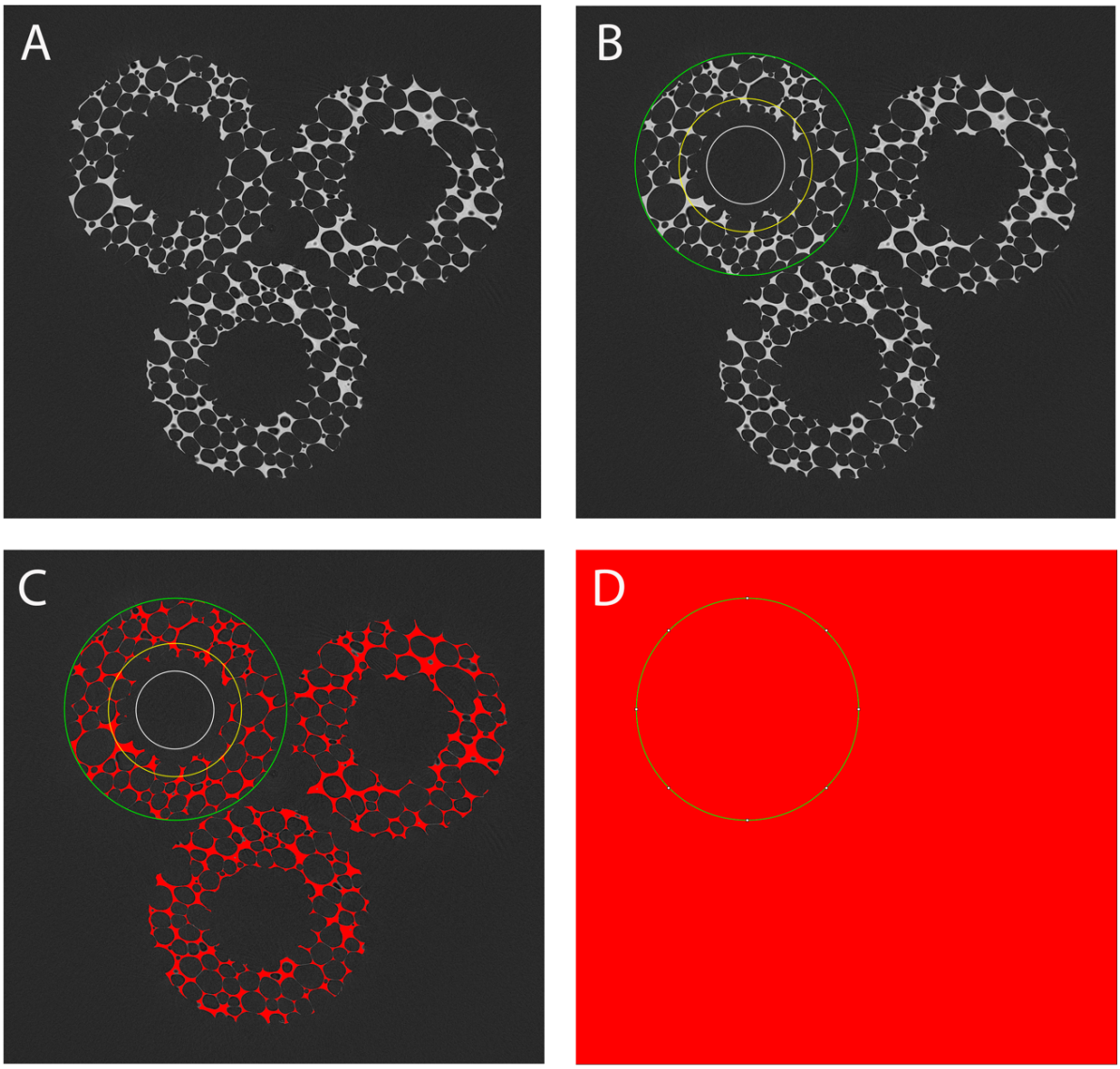

Figure 15: 12.5 PCF drilled foam specimens illustrating the measurement of foam density using ImageJ software. TIFF images are imported into ImageJ (Figure 15A), then three concentric ROIs are generated, to represent the entire specimen (green), the central 7-mm drill hole (white), and the compaction zone (yellow). The area of foam is then calculated by using thresholding to mark all the foam within the ROI (Figure 15C) and the total area (foam, empty voids) is calculated by adjusting the threshold to include all pixels in the field (Figure 15D).

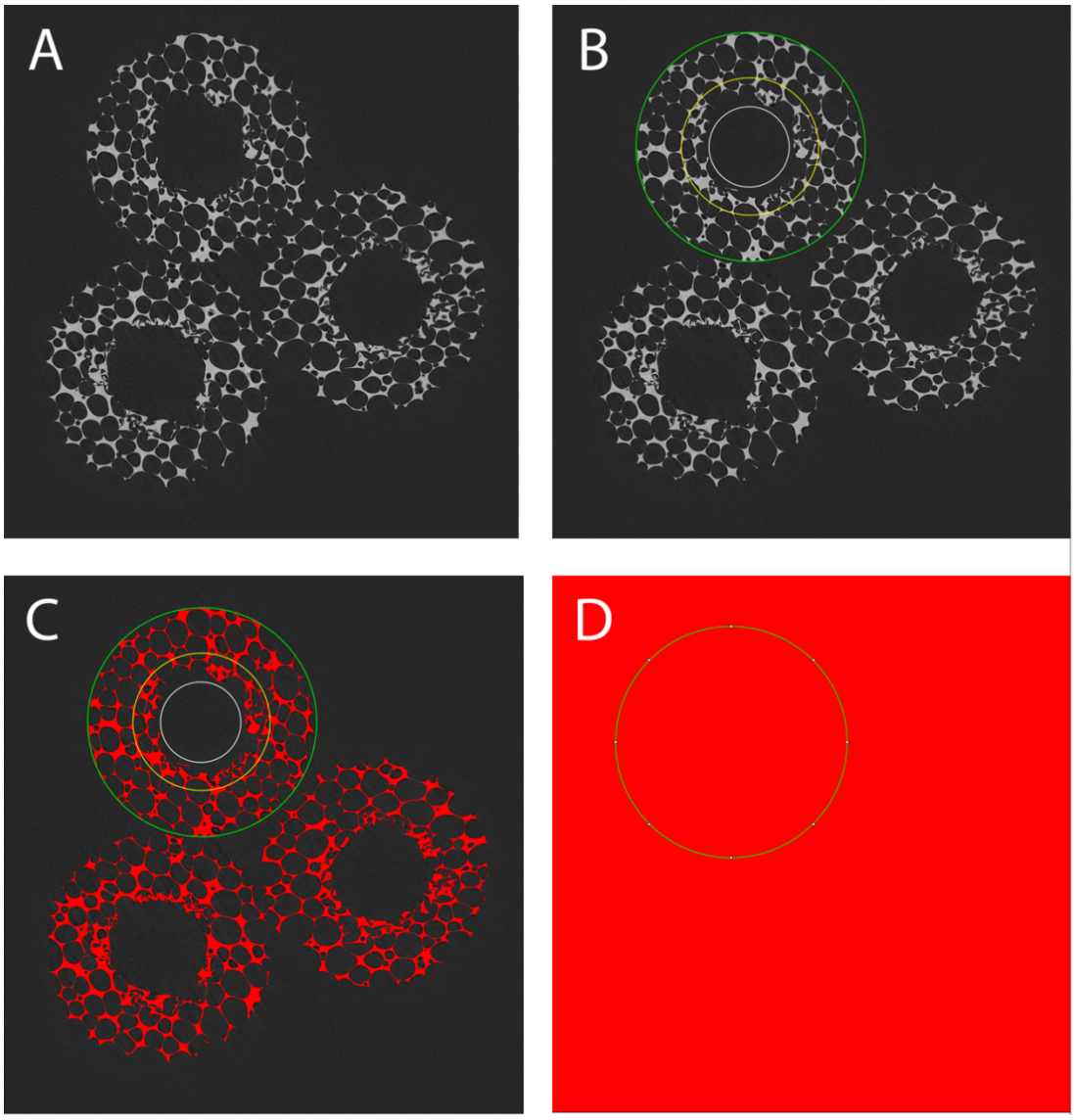

Figure 16: 12.5 PCF compacted foam specimens illustrating the measurement of foam density using ImageJ software. TIFF images are imported into ImageJ (Figure 16A), then three concentric ROIs are generated, to represent the entire specimen (green), the central 7-mm drill hole (white), and the compaction zone (yellow) (Figure 16B). The area of foam is then calculated by using thresholding to mark all the foam within the ROI (Figure 16C) and the total area (foam, empty voids) is calculated by adjusting the threshold to include all pixels in the field (Figure 16D).

Statistical methods

Sample size and power analysis

The Shapiro-Wilk test was used to assess data normality (45). The sample size for this study is based on previous studies, which consistently showed that a sample size of at least 4 specimens per group is sufficient to demonstrate statistical differences between groups when homogenous models are compared using standardized well-controlled testing conditions (21,46).

Statistical analysis

Outcome measures for **mediolateral bending** consisted of initial bending stiffness, load at 5 mm, and maximum load. Initial bending stiffness was measured to reflect the clinically relevant situation when the femoral condyle may toggle before the nail is locked with bolts. Data reported as mean and SD were compared between drilled and compacted groups across different foam densities using two-factor ANOVA followed by Tukey post-hoc tests when significant differences were identified. For the **impaction testing**, outcome measures included initial impaction stiffness in the linear range between 10 and 20 mm of displacement and maximum recorded load at 32 mm of impaction. Initial impaction stiffness was measured to reflect the synthetic cancellous bone resistance to compaction by various mandrel sizes and a 7 mm I-Loc nail. Data were reported as mean and SD and comparisons of stiffness between different mandrel sizes and I-Loc within each foam density were conducted using a repeated measures ANOVA with Tukey post-hoc tests. For the **micro-CT data**, the relationship between foam density, preparation technique (drilled versus compacted), and foam area fraction was evaluated by two-factor ANOVA with Tukey post-hoc tests. Significance was set at $p<0.05$ for all analyses.

RESULTS

Non-destructive bending (Table 1)

- *7.5 PCF*

Compared to drill specimens, compaction caused a 23% increase in initial bending stiffness and a 32% increase in load at 5 mm, however, the maximum load remained unchanged (0%). Initial bending stiffness values were 1.19 ± 0.18 N/m for the drilled group and 1.47 ± 0.25 N/m for the compacted group (ns). The load at 5 mm was measured at 5.78 ± 0.88 N in the drilled group and 7.63 ± 1.23 N in the compacted group ($p < 0.01$). Peak load measurements were 16.30 ± 0.19 N for the drilled group and 16.30 ± 1.29 N for the compacted group (ns=not significant, $p>0.05$).

- *10 PCF*

Compaction resulted in a 62% increase in initial bending stiffness, an 80% increase in load at 5 mm, and a slight, 2% rise in maximum load. Initial bending stiffness values were 2.07 ± 0.12 N/m for the drilled group and 3.34 ± 0.19 N/m for the compacted group ($p < 0.0001$). The load at 5 mm was 9.71 ± 0.40 N in the drilled group and 17.52 ± 0.74 N in the compacted group ($p<0.0001$). Maximum load was 29.51 ± 4.03 N for the drilled group and 29.99 ± 2.82 N for the compacted group (ns=not significant, $p>0.05$).

- *12.5 PCF*

Compared to drilling, compaction increased initial bending stiffness, load at 5 mm, and maximum load by 75%, 81%, and 27%, respectively. Initial bending stiffness was 2.53 ± 0.11 N/m and 4.42 ± 0.29 N/m in the drilled and compacted groups, respectively ($p<0.0001$). Load at 5 mm was 12.06 ± 0.43 N in the drilled group and 21.81 ± 1.5 N in the compacted group ($p<0.0001$). Maximum load was 38.41 ± 3.14 N and 48.62 ± 5.48 N, in the drilled and compacted groups, respectively ($p<0.0001$).

- *15 PCF*

In this group with higher density, compaction increased initial bending stiffness by 51%, load at 5 mm by 51%, and maximum load by 18%. Initial bending stiffness values were 4.41 ± 0.26 N/m for drilled specimens and 6.67 ± 0.20 N/m for compacted specimens ($p<0.0001$). The load at 5 mm was 22.02 ± 1.16 N in the drilled group and 33.26 ± 0.82 N in the compacted group ($p<.0001$), while the maximum load reached 72.82 ± 3.50 N and 85.65 ± 2.79 N, respectively ($p<0.0001$).

- *20 PCF*

The highest-density group results showed that compaction led to a 54% increase in initial bending stiffness. The load at 5 mm increased by 64%, while the maximum load saw a 34% rise. Initial bending stiffness was 4.48 ± 0.34 N/m for the drilled specimens and 6.89 ± 0.10 N/m for the compacted ones ($p<0.0001$). The load at 5 mm was 21.45 ± 1.02 N in the drilled group and 35.18 ± 0.40 N in the compacted group ($p<0.0001$), while the maximum load was 87.56 ± 1.98 N in the drilled group and 116.98 ± 7.29 N in the compacted group ($p<0.0001$).

The relationship between foam density and bending stiffness, load at 5 mm, and maximum load for drilled and compacted groups are illustrated in Figures 17-19.

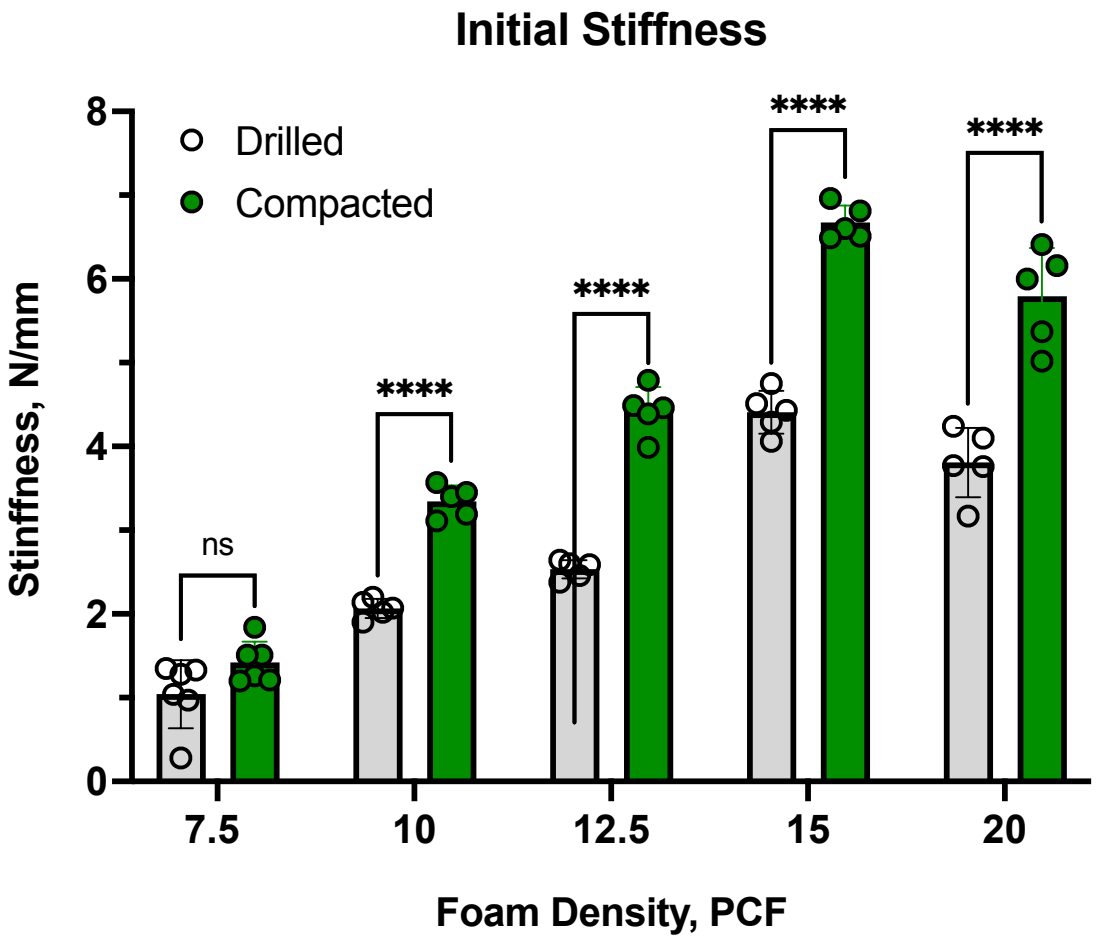

Figure 17: The relationship between foam density and initial bending stiffness, as measured by mediolateral bend testing. Asterisks denote statistically significant differences between drilled and compacted specimens for a given foam density (ns=not significant; **** $p<0.0001$).

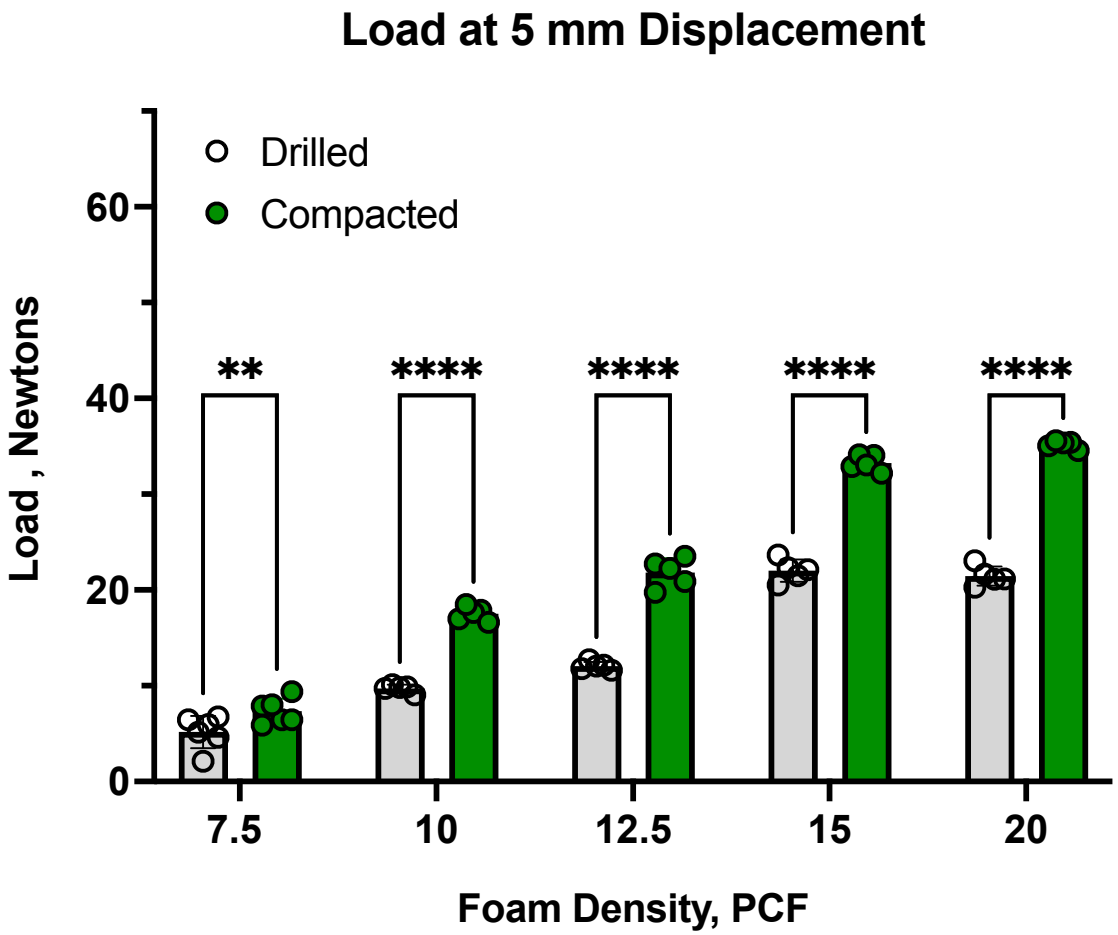

Figure 18: The relationship between foam density and load at 5 mm of nail displacement, as measured by mediolateral bend testing. Asterisks denote statistically significant differences between drilled and compacted specimens for a given foam density (** $p<0.01$; **** $p<0.0001$).

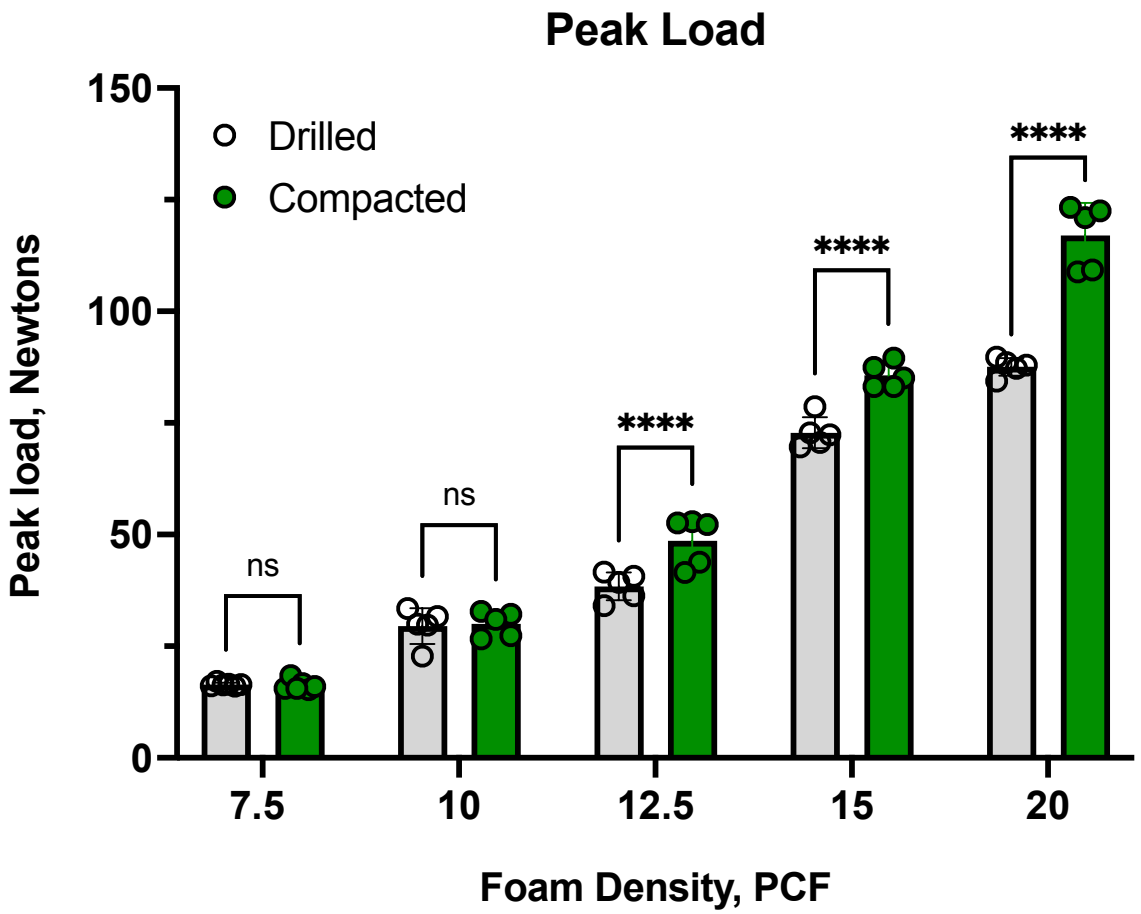

Figure 19: The relationship between different tested foam densities, preparation technique (drilled versus compacted) and peak load, as measured by mediolateral bend testing. Asterisks denote statistically significant differences between drilled and compacted specimens for a given foam density (ns=not significant; **** $p<0.0001$).

Impaction stiffness (Table 2)

- *7.5 PCF*

Data were only collected for mandrels 4 and 5. The decision was made to discontinue further data acquisition due to high variability and inconsistency in the measurements obtained. Its

extremely high porosity resulted in a sawtooth pattern in the initial impaction stiffness curve (Figure 20). This irregular pattern made it difficult to obtain consistent and reliable data.

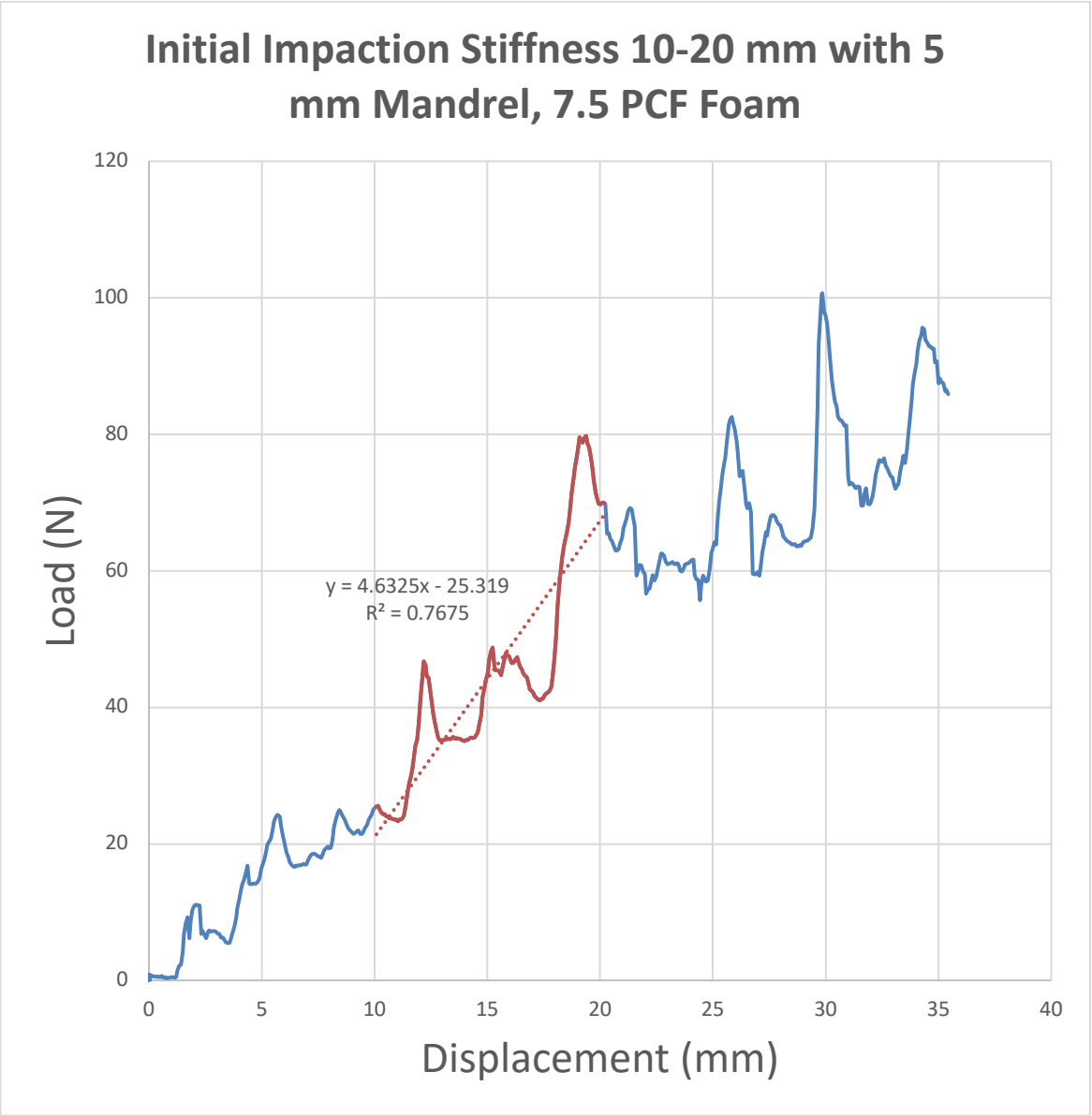

Figure 20: An example of the initial impaction stiffness curve for 7.5 PCF foam impacted with a mandrel 5. The graph illustrates the load-displacement relationship of a 7.5 PCF foam, with a focus on the 10-20 mm displacement range. The curve shows a sawtooth, rather than a linear pattern.

- *10 PCF*

At a displacement of 32 mm, the measured loads were 91.53 ± 10.1 N for mandrel 4, 153.68 ± 22.8 N for mandrel 5, 202.88 ± 17.5 N for mandrel 6, 232.33 ± 16.8 N for mandrel 7, and 177.85 ± 16.5 N for the 7 mm I-Loc nail. The initial impaction stiffness values were as follows: mandrel 4 exhibited 2.24 ± 1.0 N/m, while mandrel 5 demonstrated 6.23 ± 0.7 N/m. Mandrel 6 had an initial stiffness of 6.80 ± 0.9 N/m, and mandrel 7 measured 7.96 ± 1.8 N/m. The I-Loc initial impaction stiffness was recorded at 7.45 ± 0.6 N/m. High porosity in the foam specimens led to inconsistent mechanical behavior, resulting in sawtooth patterns in the initial impaction stiffness curves (Figure 21) rather than the typical linear region. There were incremental increases in initial impaction stiffness of 68% between mandrels 4 and 5, 32% between mandrels 5 and 6, and 15% between mandrels 6 and 7. There was a 23% decrease when comparing mandrel 7 to the I-Loc nail.

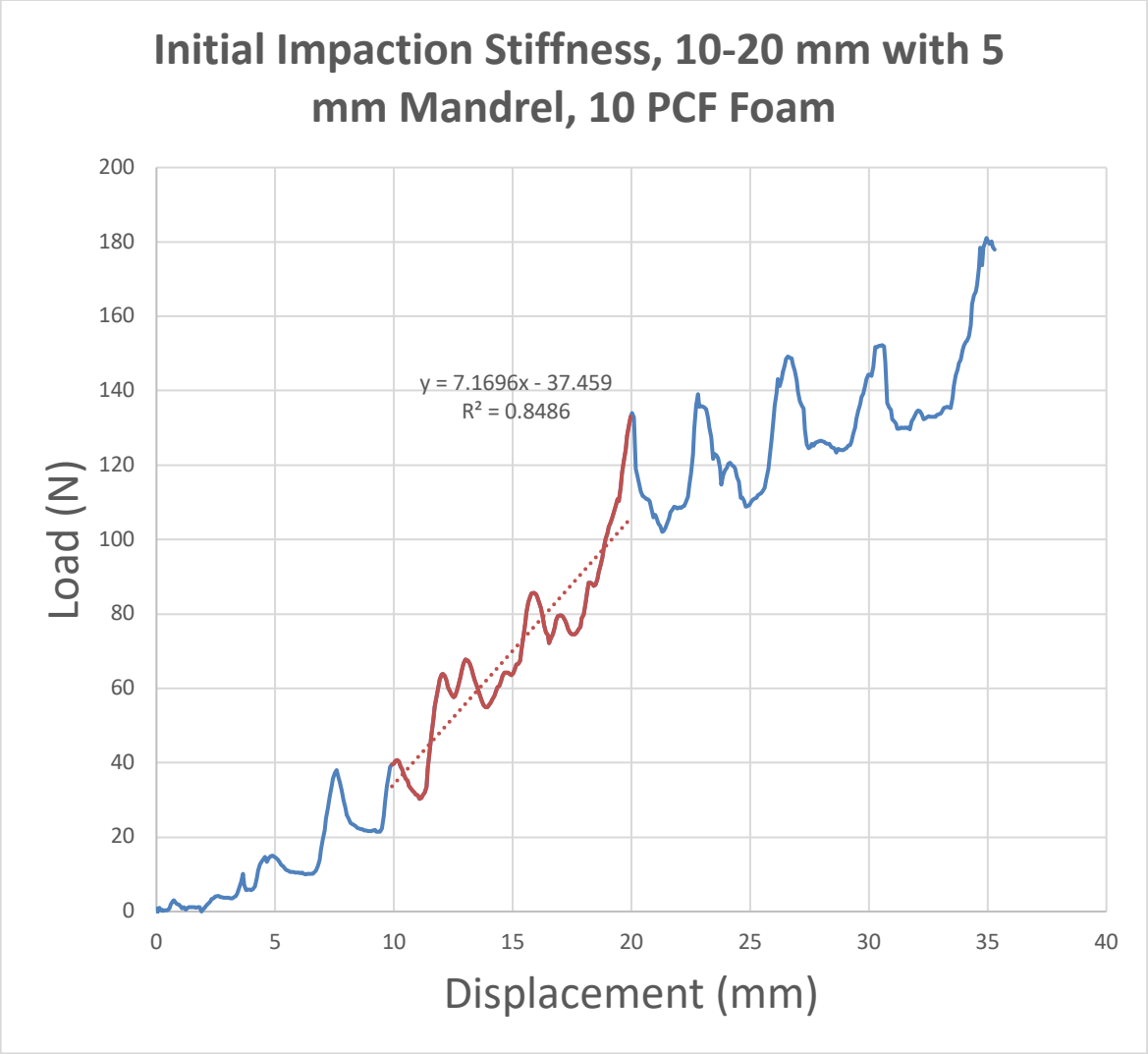

Figure 21: An example of the initial impaction stiffness curve for 10 PCF foam impacted with a mandrel 5. The graph illustrates the load-displacement relationship of a 10 PCF foam, with a focus on the 10-20 mm displacement range. The entire curve shows non-linear behavior and a sawtooth pattern.

- *12.5 PCF*

The load at 32 mm for mandrels 4, 5, 6, 7 and the I-Loc nail was 133.76 ± 16.3 N, 239.33 ± 22.2 N, 334.86 ± 24.4 N, 410.64 ± 23.2 N, 316.14 ± 4.1 N, respectively. The initial impaction

stiffness for mandrel 4 was 6.04 ± 1.1 N/m, whereas mandrel 5 had an initial impaction stiffness of 9.40 ± 0.7 N/m (Figure 22).

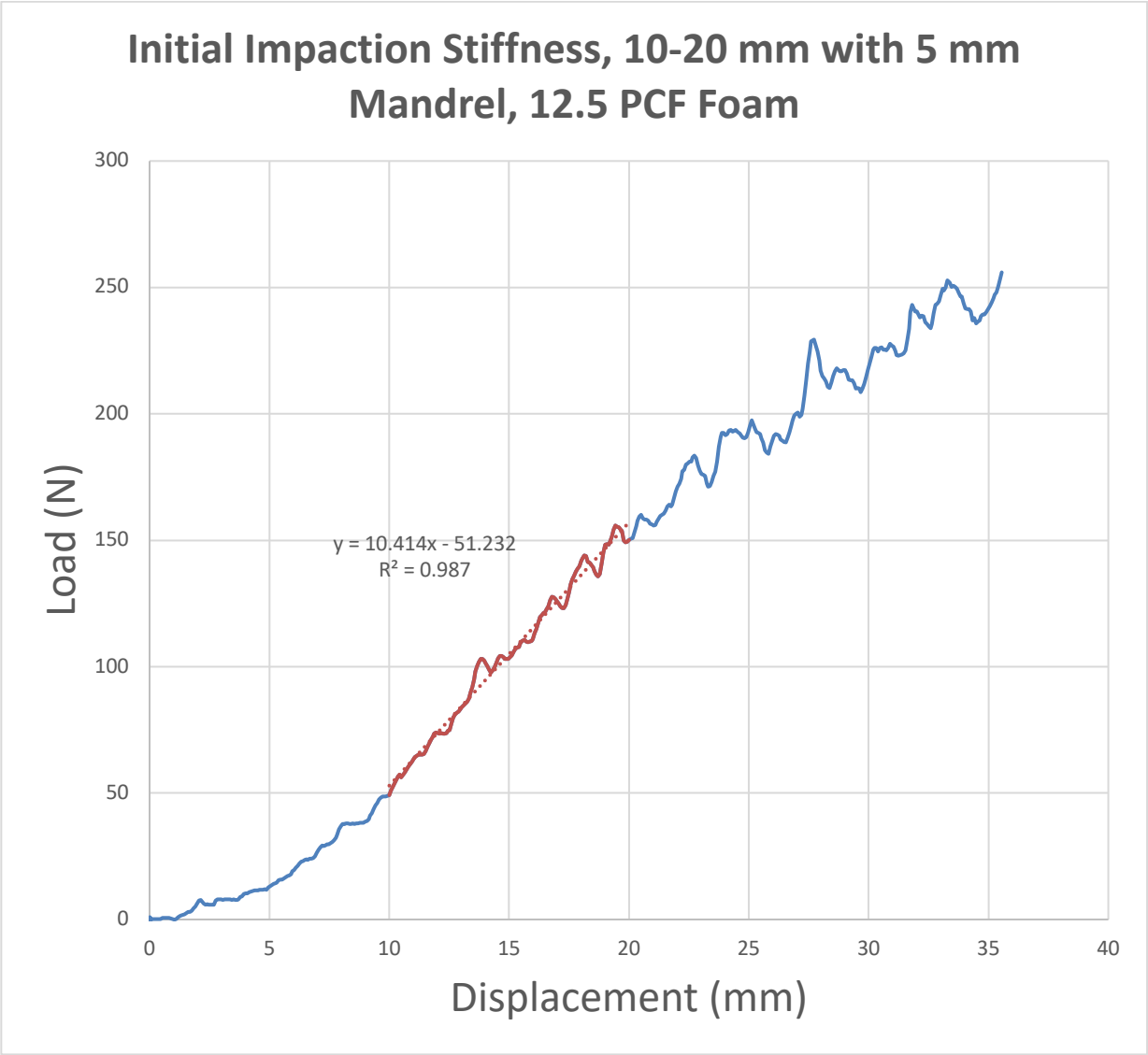

Figure 22: An example of the initial impaction stiffness curve for 12.5 PCF foam impacted with a mandrel 5. The graph illustrates the load-displacement relationship of a 12.5 PCF foam, with a focus on its linear stiffness behavior in the 10-20 mm displacement range.

Mandrels 6 and 7 demonstrated an initial impaction stiffness of 10.82 ± 1.2 N/m and 14.62 ± 1.5 N/m, respectively. The I-Loc nail showed 12.06 ± 1.1 N/m of initial impaction stiffness. The incremental increase in initial impaction stiffness was 79% between mandrels 4 and 5, 40% between mandrels 5 and 6, and 23% between mandrels 6 and 7. There was a 23% decrease in stiffness values when comparing mandrel 7 to the I-Loc nail.

- *15 PCF*

At 32 mm, the load for mandrels 4, 5, 6, 7, and the I-Loc nail measured 298.05 ± 35.2 N, 495.28 ± 15.2 N, 684.12 ± 46.3 N, 804.60 ± 40.8 N, and 636.29 ± 33.1 N, respectively. Initial impaction stiffness for mandrel 4 was 12.33 ± 1.9 N/m, mandrel 5 registered 17.26 ± 1.0 N/m (Figure 23), and mandrel 6 showed 24.12 ± 1.4 N/m. Mandrel 7 had an initial impaction stiffness of 27.85 ± 1.4 N/m, while the I-Loc nail demonstrated 23.86 ± 1.2 N/m. There were incremental increases in initial impaction stiffness of 66% between mandrels 4 and 5, 38% between mandrels 5 and 6, and 8% between mandrels 6 and 7. There was a 21% decrease when comparing mandrel 7 to the I-Loc nail.

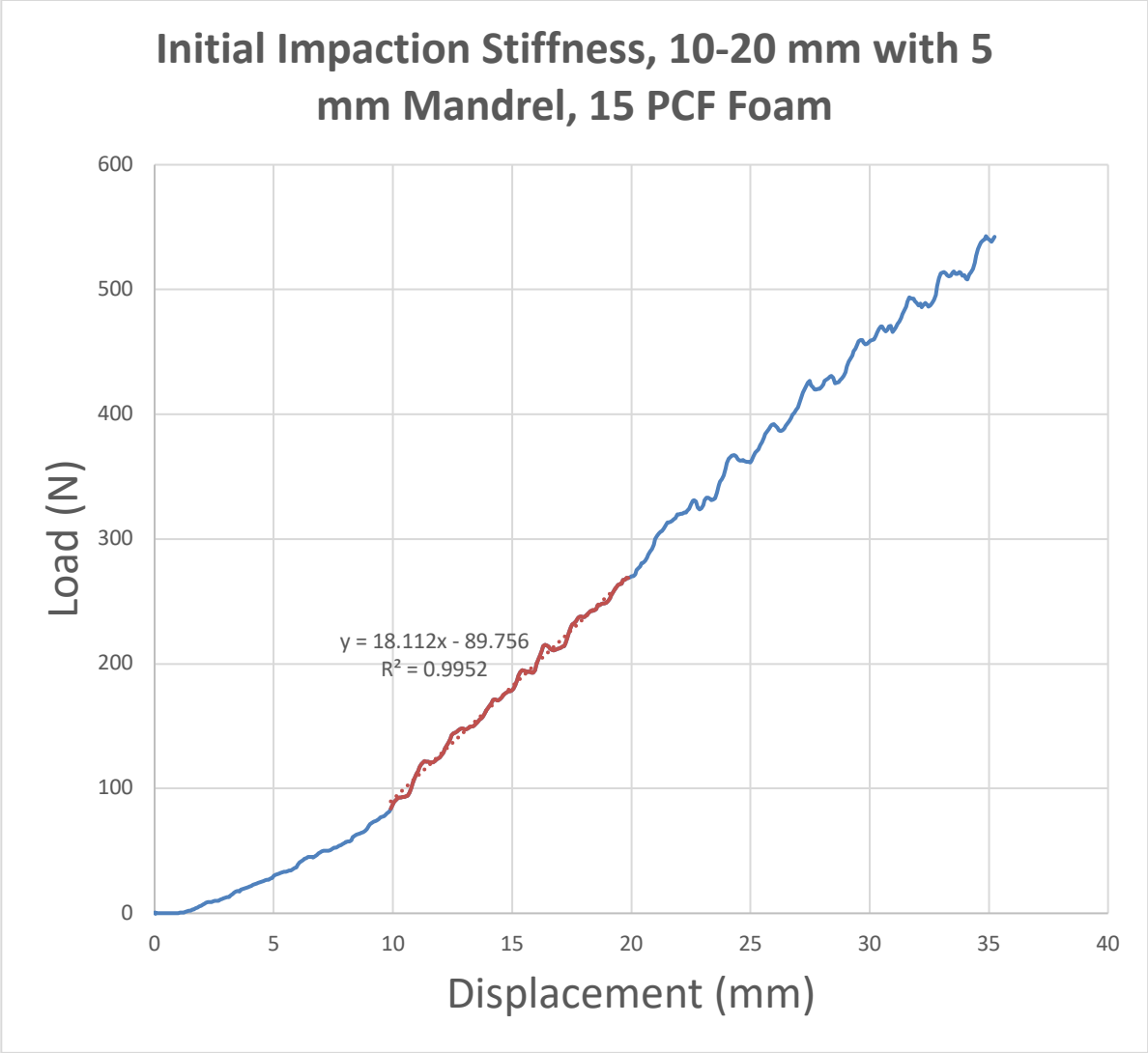

Figure 23: An example of the initial impaction stiffness curve for 15 PCF foam impacted with a mandrel 5. The graph illustrates the load-displacement relationship of a 15 PCF foam, with a focus on its linear stiffness behavior in the 10-20 mm displacement range.

- *20 PCF*

At 32 mm, the loads recorded for mandrels 4, 5, 6, 7, and the I-Loc nail were 524.79 ± 87.2 N, 927.06 ± 181.7 N, 1,377.97 ± 126.6 N, 1,490.76 ± 215.1 N, and 1,002.38 ± 123.2 N, respectively. The initial impaction stiffness measurements were 26.68 ± 6.3 N/m for mandrel 4, 43.09 ± 10.4

N/m for mandrel 5 (Figure 24), and 51.96 ± 0.6 N/m for mandrel 6. Mandrel 7 showed an initial impaction stiffness of 60.46 ± 15.6 N/m, while the I-Loc nail recorded 41.80 ± 9.7 N/m. The increase in initial impaction stiffness between mandrels 4 and 5 was 77%, between mandrels 5 and 6 was 49%, and between mandrels 6 and 7 was 8%. In contrast, there was a 33% decrease when comparing mandrel 7 to the I-Loc nail.

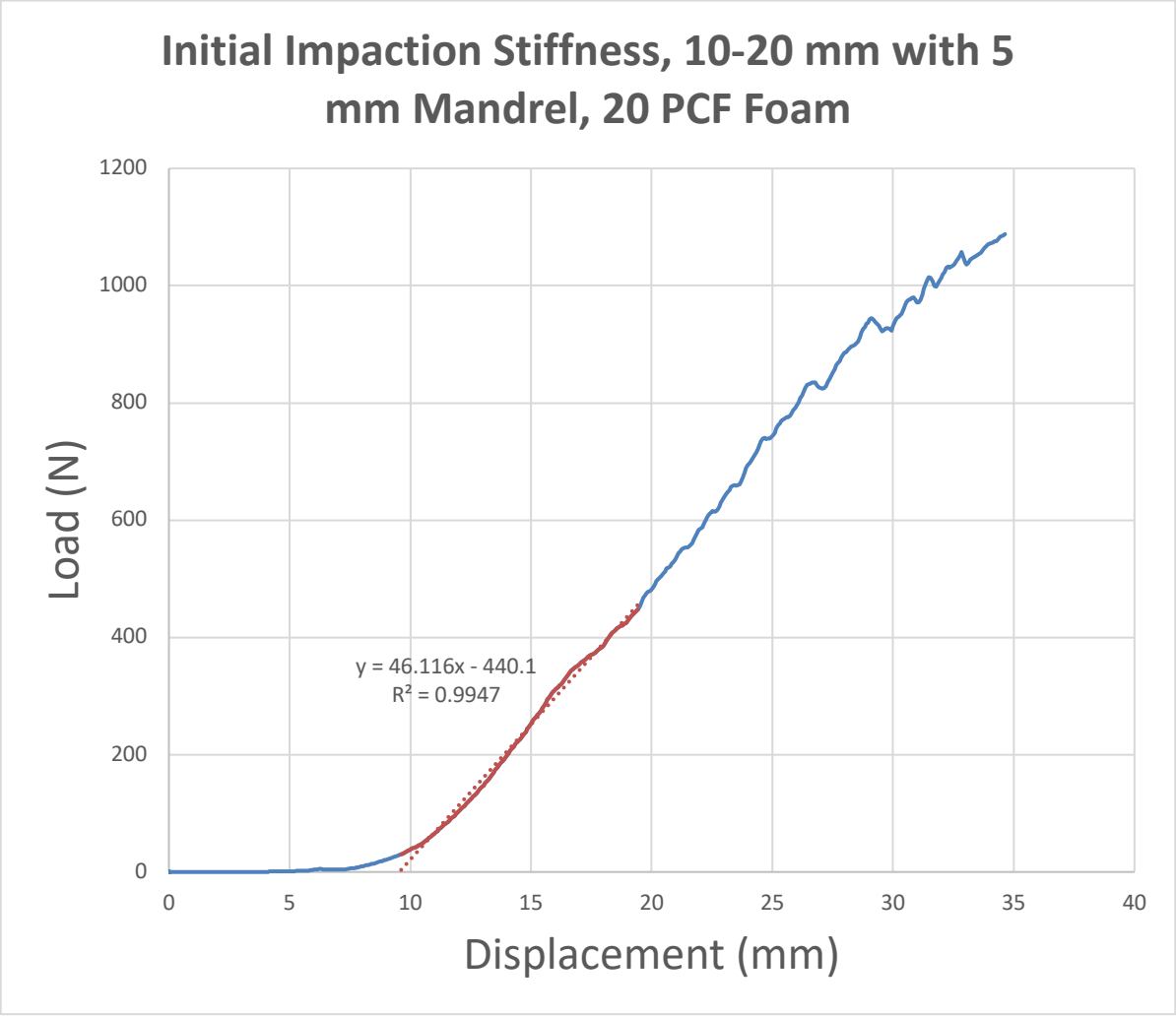

Figure 24: An example of the initial impaction stiffness curve for 20 PCF foam impacted with a mandrel 5. The graph illustrates the load-displacement relationship of a 20 PCF foam, with a focus on its linear stiffness behavior in the 10-20 mm displacement range.

The relationship between foam densities and stiffness for different sizes of mandrels and an I-Loc nail is shown in Figures 25–30.

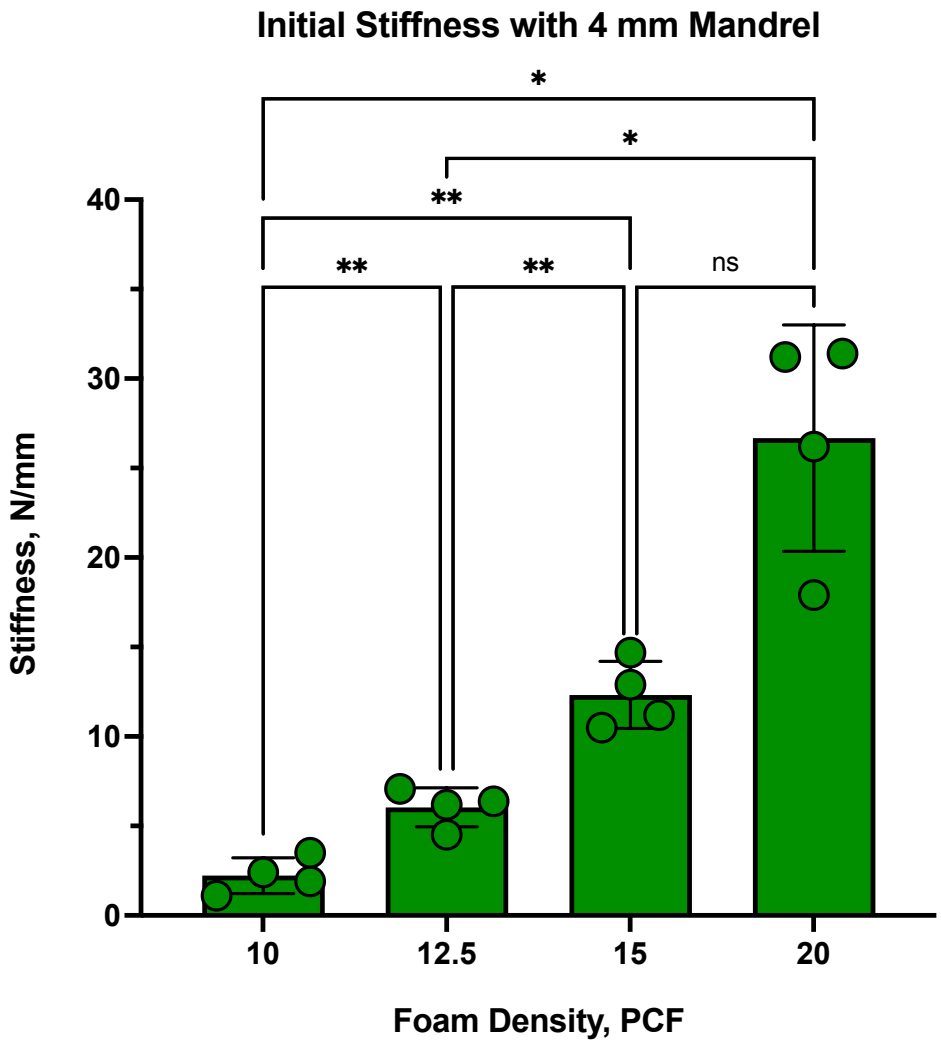

Figure 25: Initial impaction stiffness values resulting from impaction of a 4 mm mandrel into foams of different densities. Asterisks denote statistically significant differences between specimens for a given foam density (ns=not significant; * $p<0.05$; ** $p<0.01$).

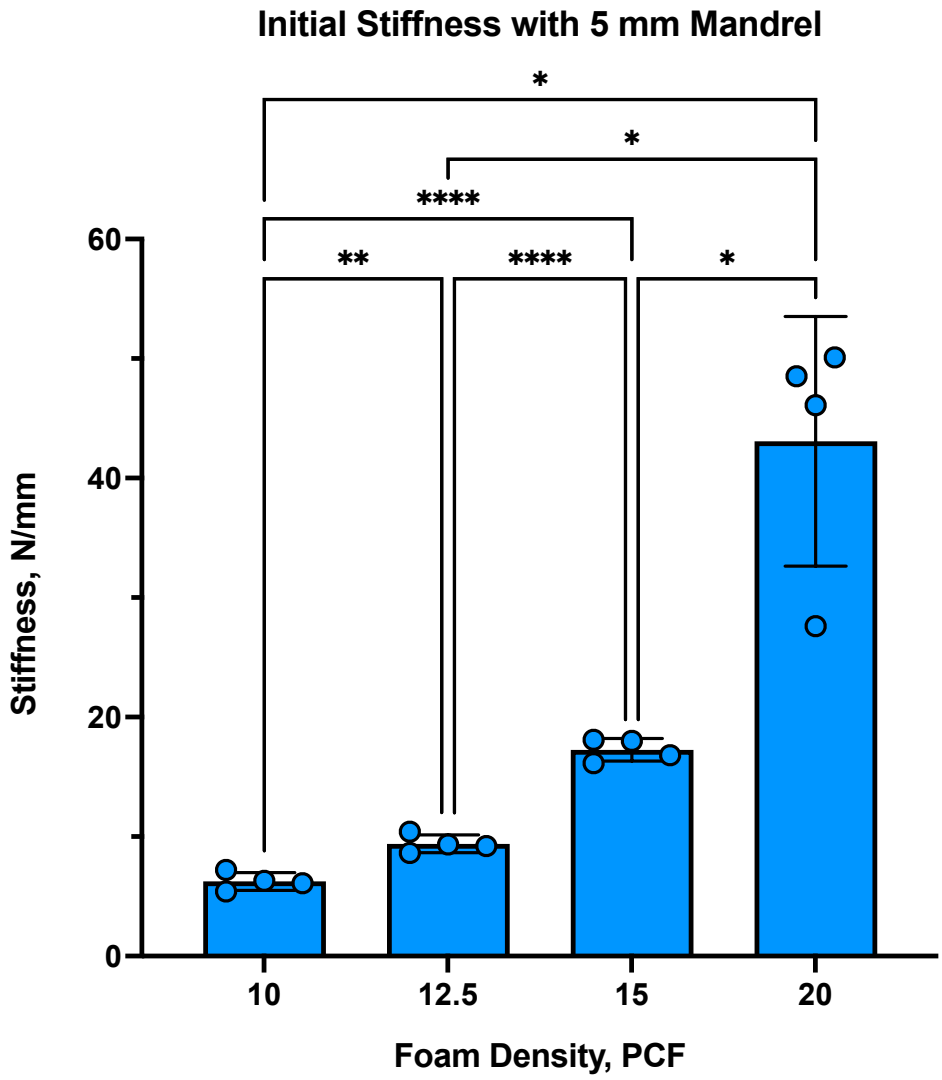

Figure 26: Initial impaction stiffness values resulting from impaction of a 5 mm mandrel into foams of different densities. Asterisks denote statistically significant differences between specimens for a given foam density (ns=not significant; * $p<0.05$; ** $p<0.01$; **** $p<0.0001$).

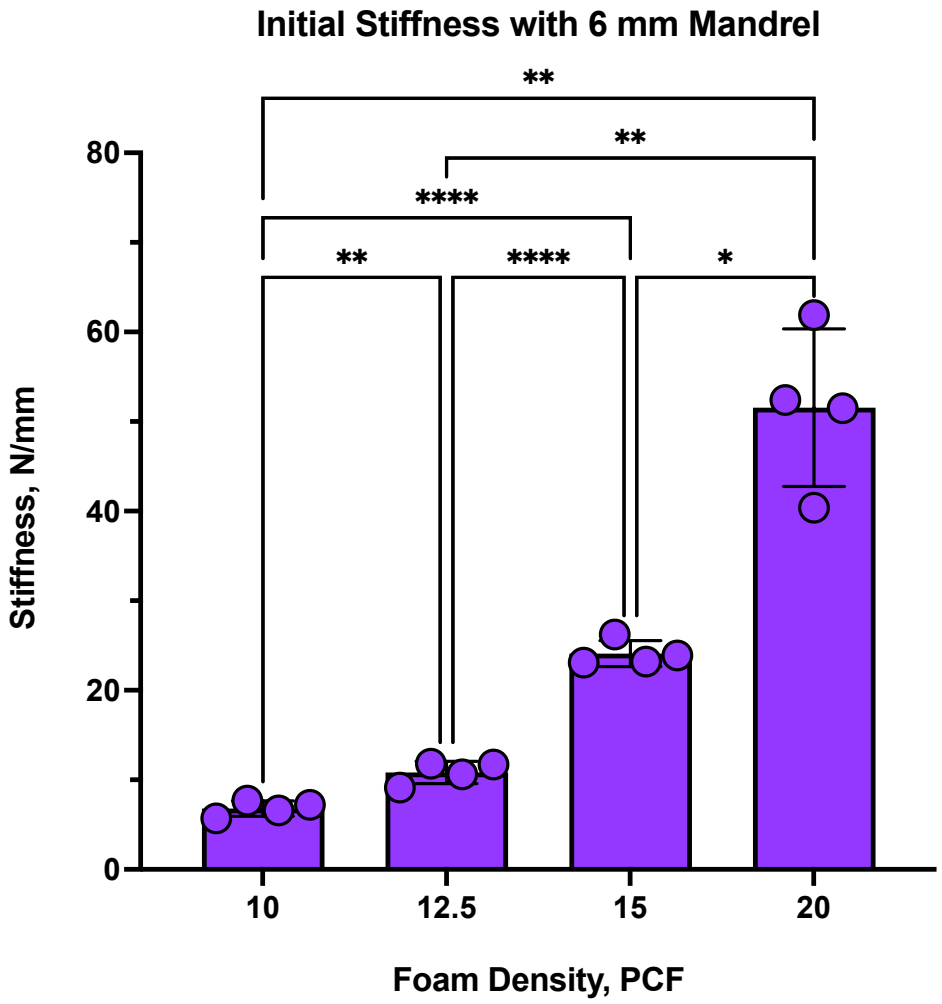

Figure 27: Initial impaction stiffness values resulting from impaction of a 6 mm mandrel into foams of different densities. Asterisks denote statistically significant differences between drilled and compacted specimens for a given foam density (* $p<0.05$; ** $p<0.01$; **** $p<0.0001$).

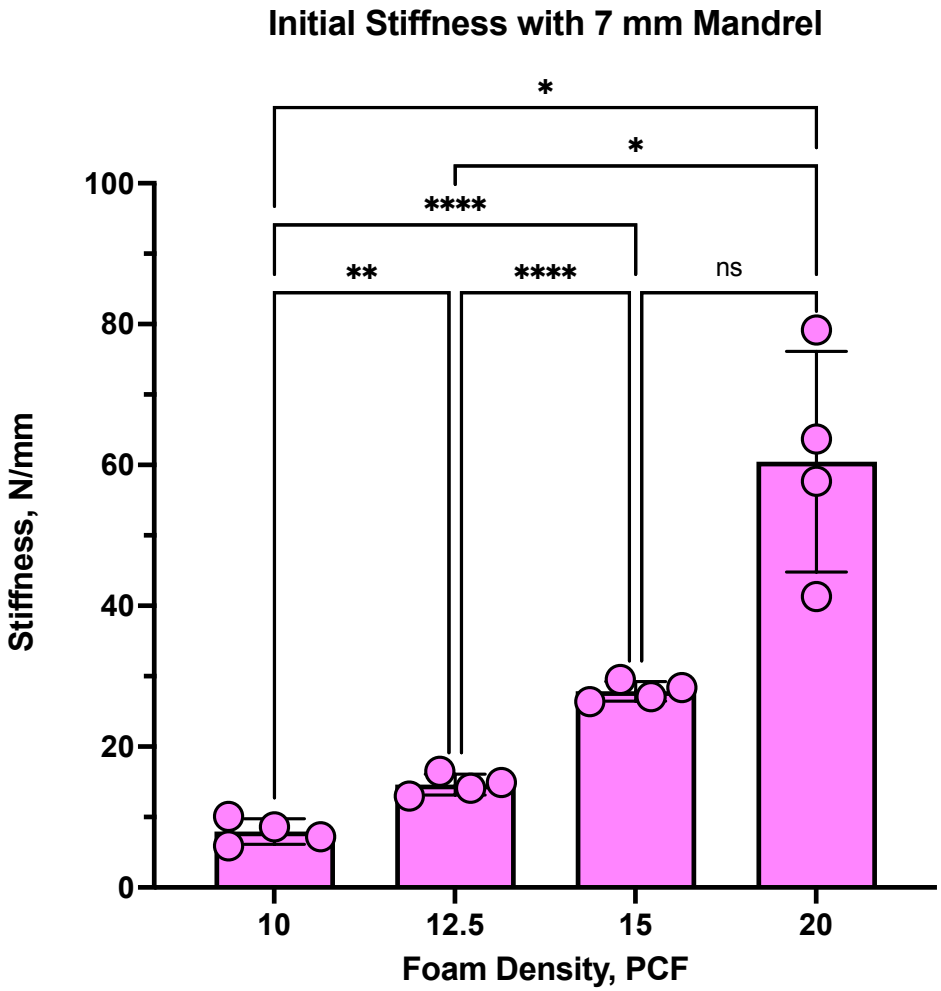

Figure 28: Initial impaction stiffness values resulting from impaction of a 7 mm mandrel into foams of different densities. Asterisks denote statistically significant differences between compacted specimens for a given foam density (ns=not significant; * $p<0.05$; ** $p<0.01$; **** $p<0.0001$).

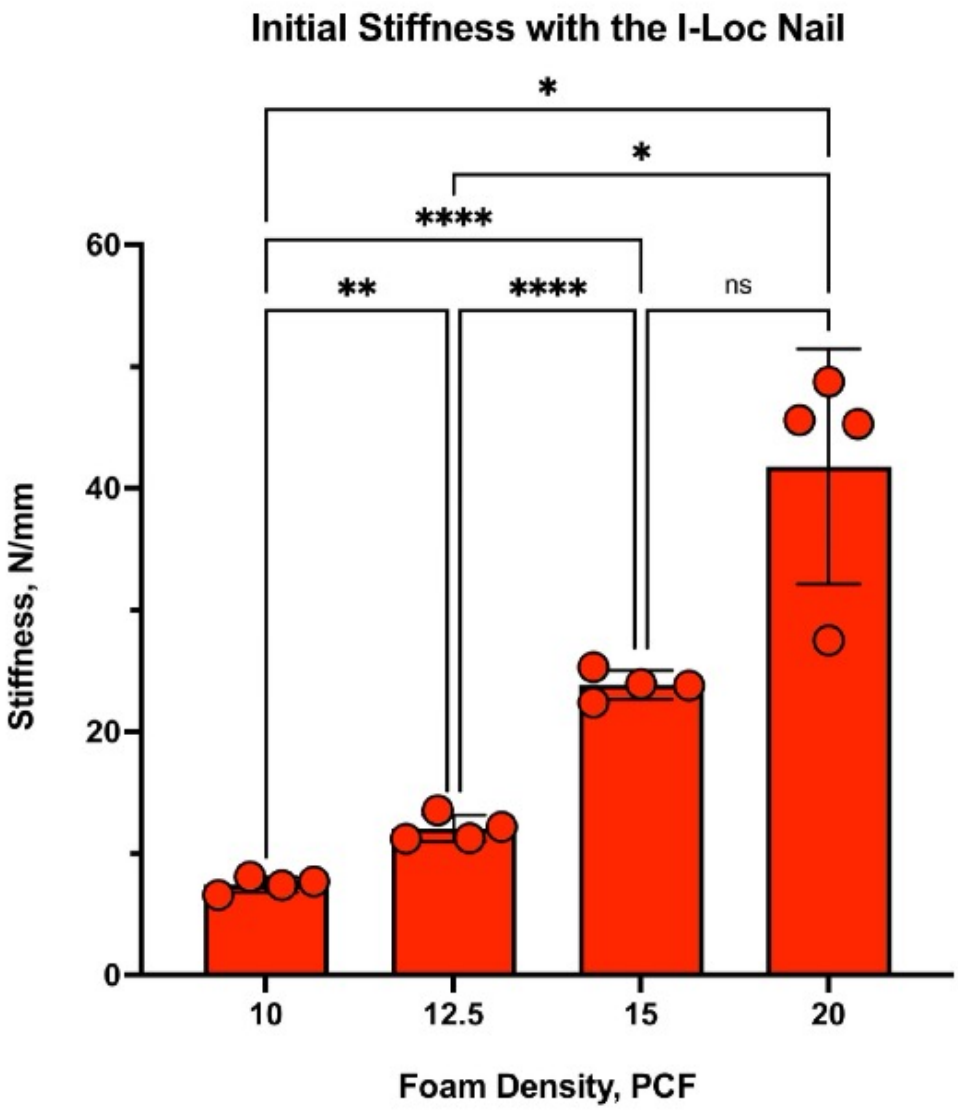

Figure 29: Initial impaction stiffness values resulting from impaction of a 7 mm I-Loc nail into foams of different densities. Asterisks denote statistically significant differences between drilled and compacted specimens for a given foam density (* $p<0.05$; ** $p<0.01$; **** $p<0.0001$).

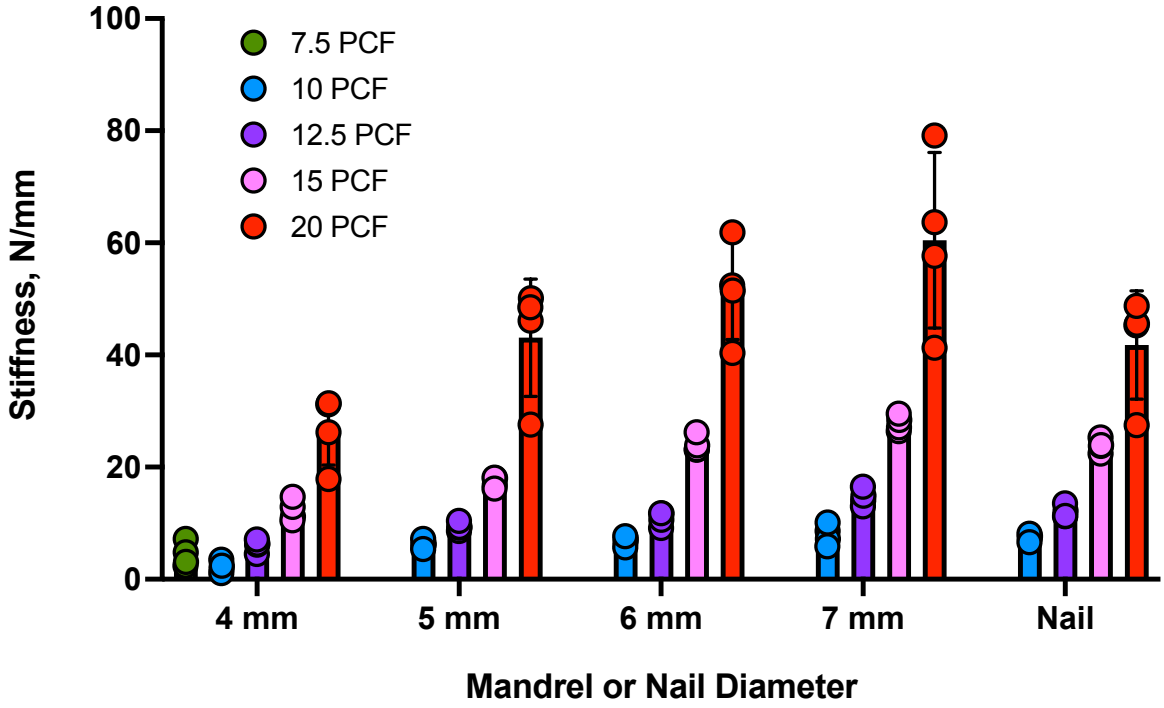

Figure 30: The relationship between various mandrel sizes/I-Loc nail and stiffness across different foam densities.

Micro-CT scans (Table 3)

Results from micro-CT scans and measurements of the compaction zone vs non-compaction zone showed that as foam density increases from 7.5 PCF to 20 PCF, there is a clear trend of increasing area fraction of foam in both zones (Figures 31-36 and – Table 3). For the lowest density foam (7.5 PCF), there is minimal difference between drilled and compacted specimens. As density increases (10 PCF and above), a more pronounced difference between drilled and compacted samples is seen, especially in the compaction zone (Table 3). Additionally, compacted foams generally show higher area fractions, particularly in the compaction zone, indicating that the compaction process is densifying material in this region.

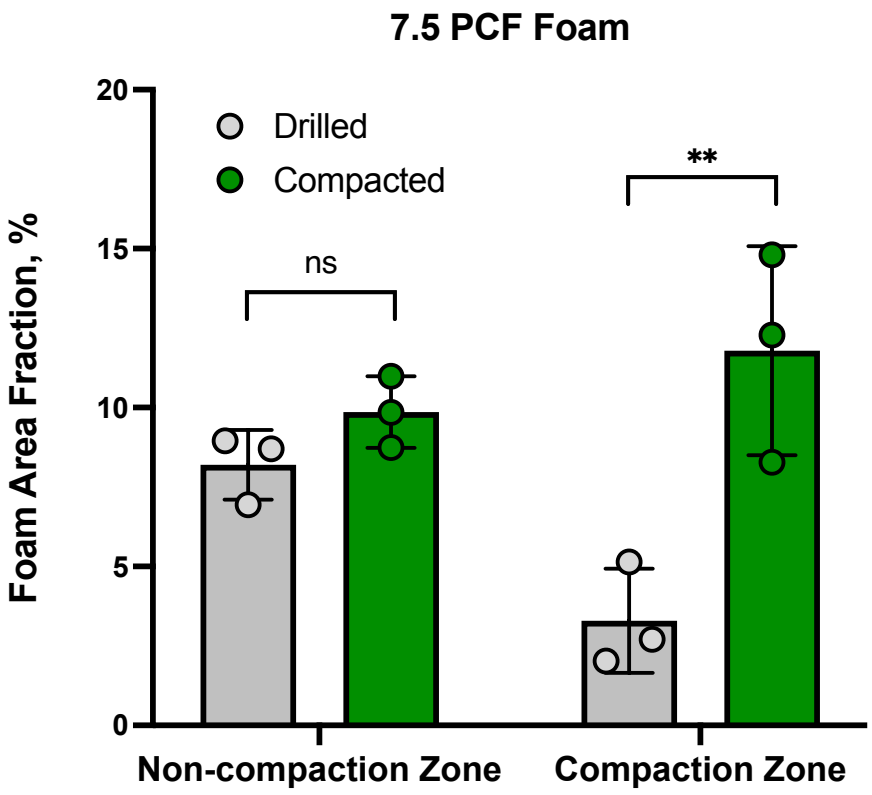

Figure 31: Comparison of foam area fraction for compacted and drilled 7.5 PCF foam, across two different areas of the foam: the compaction zone and the surrounding non-compaction zone. Asterisks denote statistically significant differences between drilled and compacted specimens for a given foam density (ns=not significant; ** $p<0.01$).

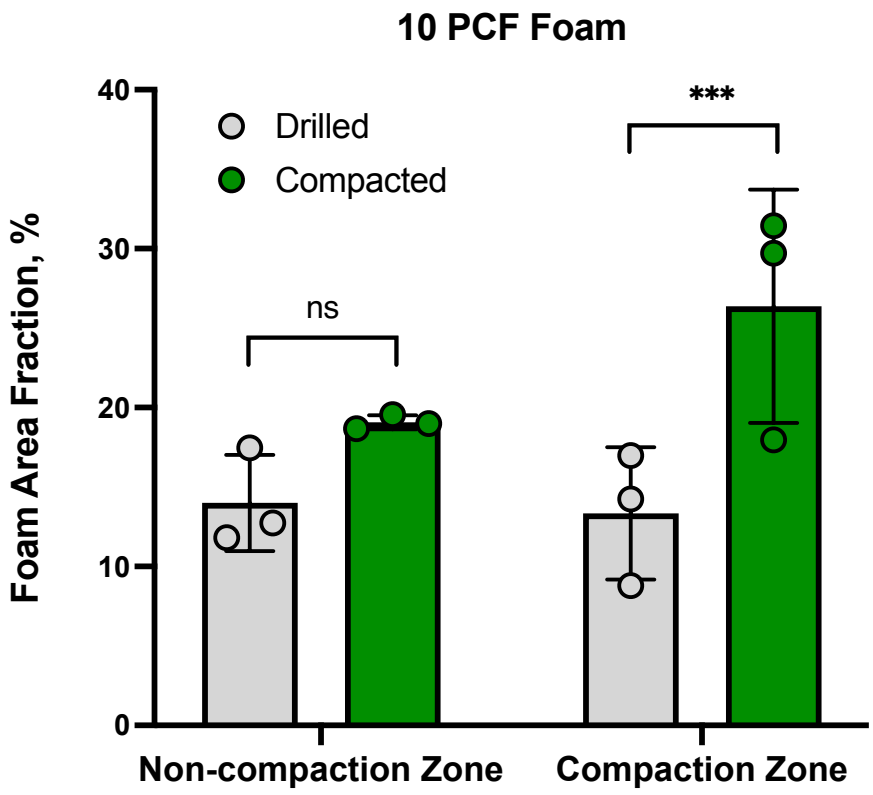

Figure 32: Comparison of foam area fraction for compacted and drilled 10 PCF foam, across two different areas of the foam: the compaction zone and the surrounding non-compaction zone. Asterisks denote statistically significant differences between drilled and compacted specimens for a given foam density (ns=not significant; *** $p<0.001$).

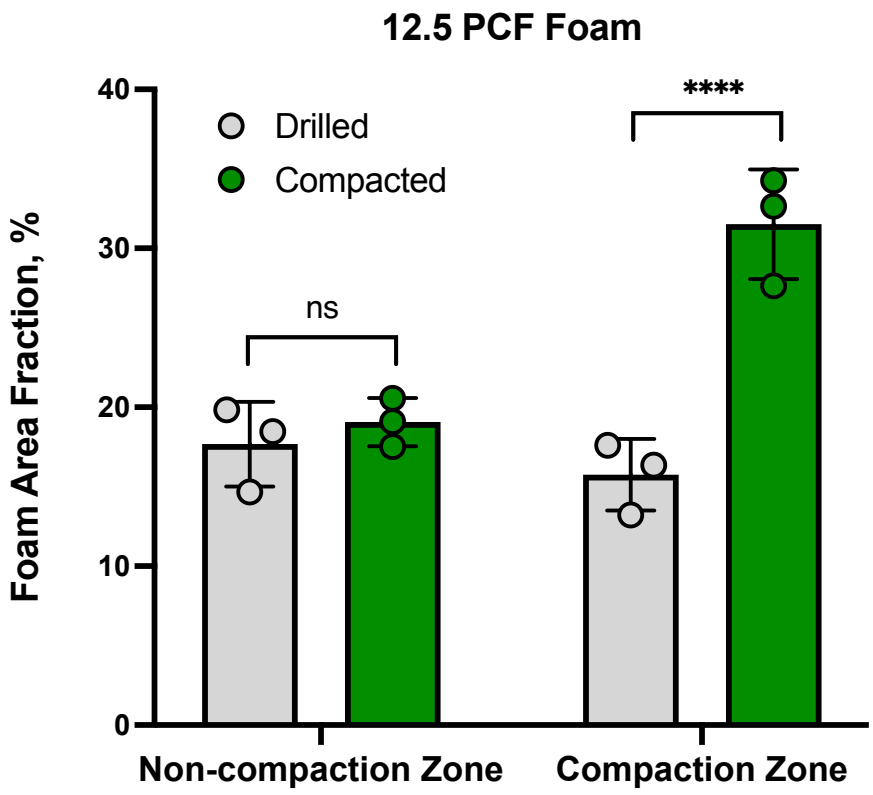

Figure 33: Comparison of foam area fraction for compacted and drilled 12.5 PCF foam, across two different areas of the foam: the compaction zone and the surrounding non-compaction zone. Asterisks denote statistically significant differences between drilled and compacted specimens for a given foam density (ns=not significant; **** $p<0.0001$).

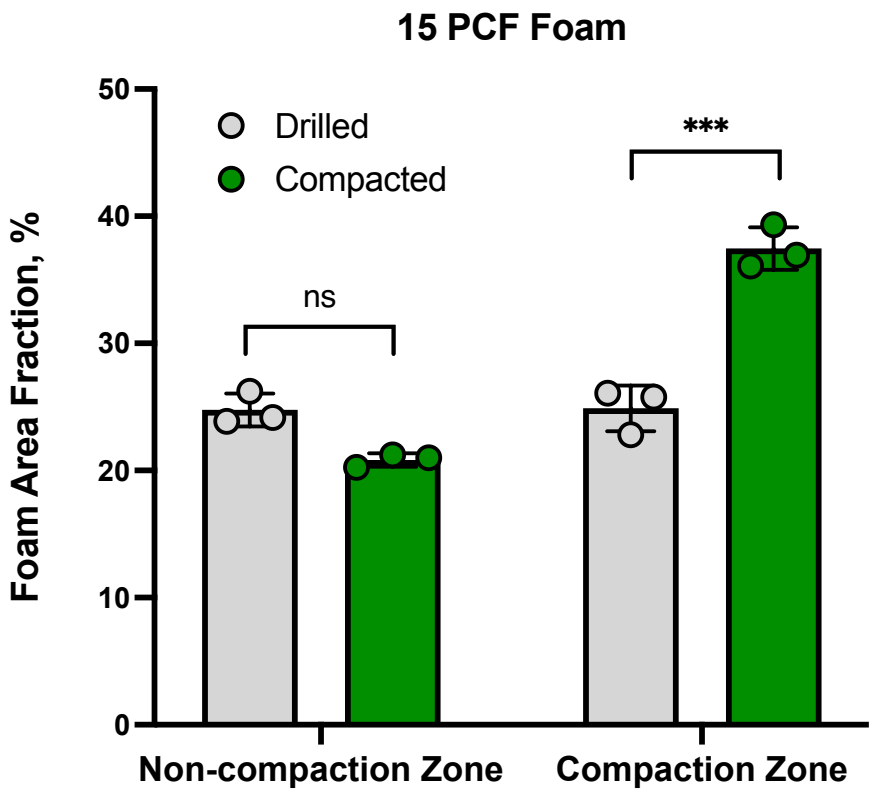

Figure 34: Comparison of foam area fraction for compacted and drilled 15 PCF foam, across two different areas of the foam: the compaction zone and the surrounding non-compaction zone. Asterisks denote statistically significant differences between drilled and compacted specimens for a given foam density (ns=not significant; *** $p<0.001$).

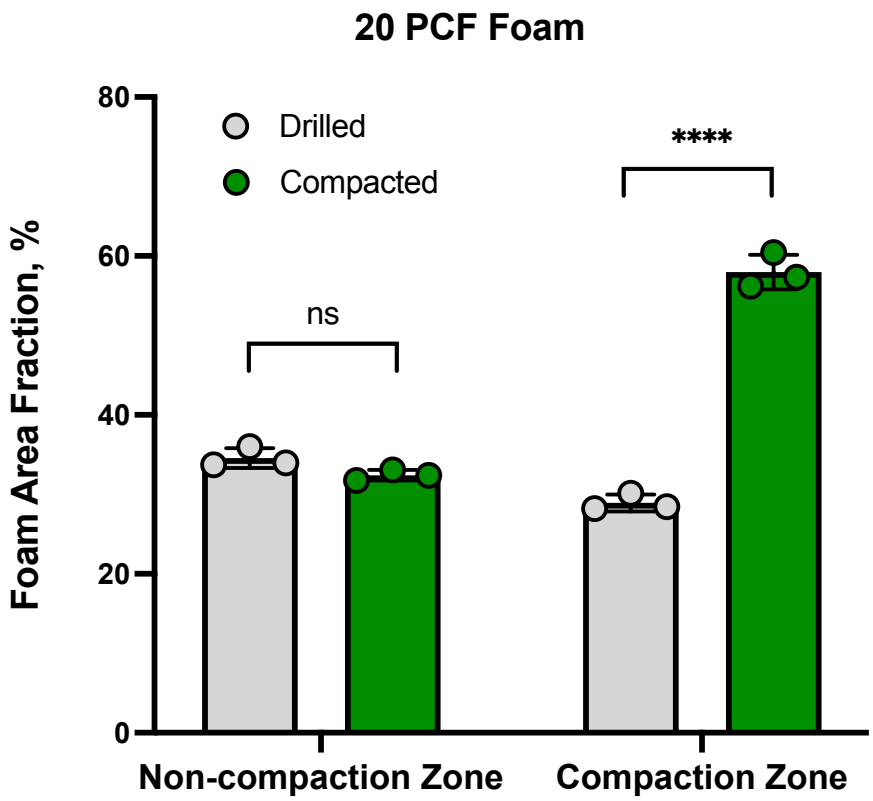

Figure 35: Comparison of foam area fraction for compacted and drilled 20 PCF foam, across two different areas of the foam: the compaction zone and the surrounding non-compaction zone. Asterisks denote statistically significant differences between drilled and compacted specimens for a given foam density (ns=not significant; **** $p<0.0001$).

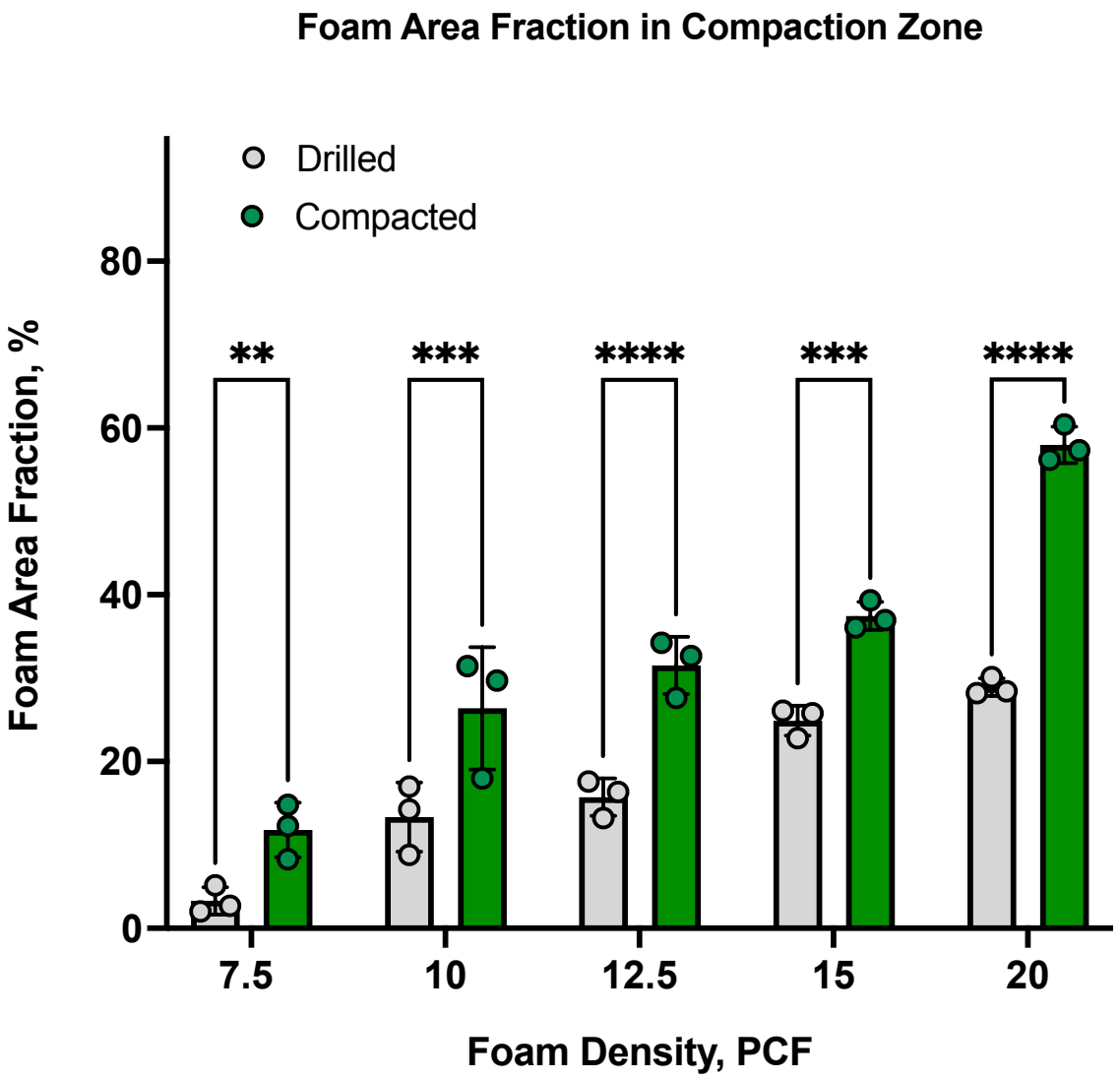

Figure 36: Comparison of foam area fraction between compacted and drilled samples across different foam densities. Asterisks denote statistically significant differences between drilled and compacted specimens for a given foam density. Asterisks denote statistically significant differences between drilled and compacted specimens for a given foam density (** $p<0.01$; *** $p=0.001$; **** $p<0.0001$).

DISCUSSION

This study demonstrates that cancellous bone compaction is an effective technique for improving the immediate, intraoperative mechanical stability of an I-Loc nail used in a simulated DFV correction in bone models of different densities. Cancellous bone compaction significantly increased the stiffness, resistance to bending, and peak load sustained by the simulated bone-nail interface. These changes in mechanical performance were underpinned by significant changes in the microstructure of foam within a compacted area around the central drill hole. The improvement in mechanical properties was associated with an increase in the density (area fraction) of foam in the compaction zone.

With conventional cancellous drilling, bone is removed from the femoral metaphysis while the mechanical properties of the cancellous envelope are maintained. When using an interlocking nail to correct DFV, forces applied to the nail prior to locking result in a potentially deleterious bending moment being applied to the distal femoral construct. This could affect the integrity of the cancellous tunnel in which the nail is inserted, particularly in the presence of a weak cancellous envelope. Secondary loss of alignment, and therefore incomplete DFV correction, could be associated with an increased risk of post-operative patellar re-luxation. In contrast, compacting cancellous bone prior to nail insertion provides a more secure interlock at the bone-implant interface. Furthermore, cancellous compaction preserves the native bone stock and increases the density of the original cancellous bone scaffold *in situ*. This in turn allows for superior immediate primary fixation stability until the insertion of the locking bolts provides final stable fixation.

Primary implant stability depends on multiple factors, including surgical technique, implant design, bone density, and bone quantity or mass (47,48). Recognizing the importance of these factors, recent research has focused on the preparation of the implant bed. Various methods have

been investigated for preparing the implant site, including the use of bone compactors, osseodensification drills, bone expanders, and osteotomes (49-52). While drilling with a smaller pilot hole is the most common technique used for this purpose, it has limitations. It only improves primary stability in normal bone and removes bone material, which may have a negative effect on bone healing (53,54). Additionally, undersized drilling can cause excessive compression and may lead to bone ischemia, potentially compromising implant stability (55). New techniques have been developed to increase bone density around the implant. These include osseodensification, which employs specialized drills that can compress and densify bone when rotated counterclockwise. Alternatively, manual bone compactors can be used to gradually expand the implant site utilizing bone elasticity to slowly reshape the trabeculae (49,56). In our study, we used a manual bone compaction technique that employs progressively larger mandrels. It has been shown that this technique offers a more conservative approach to conventional drilling (49). The technique preserves bone by maintaining a larger amount of existing bone rather than removing it. Additionally, the process involves a gradual compression of bone trabeculae that can be controlled by the surgeon throughout the procedure. Compaction can be particularly beneficial in cases where bone quality and quantity are low or suboptimal. By preserving the native bone, this approach may create a more favorable environment for osseointegration. Furthermore, mandrels used in this technique are simple, cost-effective, and user-friendly adding to the overall advantages of this method.

Our results showed that, across all densities, the compacted groups showed consistently higher interfacial mediolateral bending stiffness and strength compared to the drilled groups. This indicates a more robust bone-implant construct that resists nail toggling or angular micromotion. The difference in initial bending stiffness and load at 5 mm between both drilled and compacted

groups became more pronounced as density increased but was still evident even at the lowest tested density (7.5 PCF). The load at 5 mm displacement was from 32% to 81% higher with compaction across all density groups, suggesting substantially more resistance to early loss of reduction. Our data suggests that compaction consistently improved initial bending stiffness and load at 5 mm, which is beneficial for immediate intra-operative (pre-locking) stability. This post-compaction enhanced stability agrees with findings from other studies (57,58) and suggests it could be useful in improving DFV correction by potentially reducing complications related to intra-operative instability occasionally seen with conventional drilling. Under mediolateral bending, the compacted group showed a 54% increase in initial bending stiffness compared to drilled specimens, and approximately twice the load required to induce 5 mm of displacement, corresponding to ~ 1.8° of angulation. While compaction demonstrated a positive effect on maximum load across most density groups, with a rise varying from 2% to 34% (10-20 PCF), 7.5 PCF foam showed no effect. In the low-density foams, the increase was either absent (7.5 PCF foam) or minimal at 2% (10 PCF foam) indicating that compaction had limited influence on the ultimate strength of less dense materials. Conversely, as density increased, the benefits of compaction became more pronounced. For maximum load, the 12.5 PCF group showed a 27% increase in maximum load, the 15 PCF group exhibited an 18% improvement, and the highest density group (20 PCF) demonstrated the most significant enhancement at 34%. Overall, the most notable compaction effect was often observed in the mid-range foam densities (10-12.5 PCF), indicating that compaction may be particularly beneficial for animals with normal cancellous bone and those with mildly osteoporotic cancellous bone. In higher-density specimens (15 and 20 PCF), compaction showed consistent improvements across all parameters, suggesting potential benefits even for sclerotic cancellous bone. However, in very low-density specimens (7.5 PCF), although

initial bending stiffness increased, the lack of change in maximum load implies that compaction alone may not be sufficient to enhance overall bone strength in cases with severe osteoporosis or that it may be less effective during prolonged loading in the low-quality bone than in normal or sclerotic bones. Our results provide strong support for the mechanical advantages of compaction over drilling in bone preparation across multiple parameters. The data suggest potential for improved clinical outcomes, however, we acknowledge that further research is necessary to fully understand the biological and long-term clinical implications of this technique.

From a clinical perspective, the most relevant data are initial bending stiffness and the early load at 5 mm (<2° of angular nail displacement), as these conditions closely reflect the mechanical environment before stabilization occurs. In contrast, maximum load, mid-, and final bending stiffness are of lesser importance since the locking mechanism such as locking bolts would typically be placed before these higher loading conditions are reached. As a result, although computed, mid- and final bending stiffness were not reported here since their impact on clinical outcomes is minimal compared to the early mechanical response.

Our impaction results showed that there is a general trend of increasing load at 32 mm as the mandrel diameter increases from 4 mm to 7 mm. The I-Loc nail had a lower load at 32 mm compared to the 7 mm mandrel and this can be explained by the similar diameter of the 7 mm mandrel and the I-Loc nail. There was a clear trend of increasing impaction stiffness from 4 mm mandrel to 7 mm mandrel. This progression shows approximately a 2.5x increase in stiffness. Additionally, our data showed that 6 mm and 7 mm mandrels as well as a 7 mm nail provide the highest impaction stiffness. These impaction test results indicate that increased mandrel size up to the final I-Loc nail improved stability and provided better fixation and anchoring in compacted samples. The negative percentage change from mandrel 7 to I-Loc suggests that the I-Loc nail does

not outperform the largest mandrel in this study, likely due to their similar sizes. An argument could be made that potentially transitioning directly from a 6 mm mandrel to a 7 mm I-Loc nail without using a 7 mm mandrel may be a feasible option. However, it is important to note that the I-Loc nail still performed better than mid-sized mandrels. Yet, another clinically relevant consideration is that, should mandrel impaction become too challenging early on (a subjective evaluation based on the surgeon's experience), the surgeon could decide to revert to drilling at a smaller diameter before resuming compaction. Future clinical studies are warranted to shed some light on this theory.

The micro-CT scans provided compelling visual evidence of the effects of compaction on foam specimens of varying densities. These scans revealed significant differences between drilled and compacted groups. In the compacted foams, a distinct ring of densification was visible expending out from the central pilot hole. This compacted region was the result of the compression and redistribution of foam material when mandrels of increasing sizes were inserted into the central pilot hole. The presence of this dense ring is particularly significant as it suggests a localized increase in material density, which contributes to enhanced structural property and thus stability at the foam-implant interface.

The intensity and visibility of this compaction effect appear to correlate with foam density. In the lower density foams (7.5 and 10 PCF), the compaction ring was less pronounced and often harder to discern. This was particularly evident in the 7.5 PCF samples, where the foam structure appears more open and less organized around the center. Furthermore, lower density foams feature larger pore sizes and a more open and irregular cellular structure. Therefore, larger pores in lower density foams may require more significant compaction to create a visible dense region. Although the visual evidence of compaction is less pronounced in low density foams, our biomechanical

testing and results proved that the compaction process still yields significant mechanical benefits. As discussed earlier, the compaction effect on immediate, pre-locking stability of the bone-implant interface was consistently observed across all foam densities, including those where the compacted region was less apparent in the micro-CT scans.

Micro-CT scans showed that as foam density increases, as seen in the 12.5 PCF and higher density specimens, the compaction effect becomes more pronounced, with a more clearly defined and wider dense ring around the central hole. The dense ring created by compaction provides increased surface area for contact and improved mechanical stability between the implant and the surrounding material, which could translate to better initial, pre-locking fixation and potentially improved long-term integration of bone-implant interface in clinical settings. Taken as a whole, these results support and provide an explanation for the observation of enhanced mechanical properties in the compacted specimens.

Mediolateral bending was selected over craniocaudal bending primarily to assess varus and valgus malalignment of the distal bone fragment and to simulate the biomechanical forces associated with angular femoral deformities. Varus deformity refers to the inward angulation of a bone, while valgus deformity describes the outward angulation. These deformities primarily affect the alignment of the limb in the mediolateral plane. Additionally, Dejardin et al (46) suggested that the structural characteristics of ILNs make them inherently more susceptible to failure when stressed transversally rather than in the sagittal plane. During ambulation, joint flexion and extension may partially mitigate loads in the sagittal plane, potentially reducing stress on the implants in this direction. Mid-and low-level joints, primarily operate as hinge joints. Their structure inherently limits movement in the transverse plane. Consequently, when forces act in this plane, as occurs with varus or valgus stress, the implant is more likely to bear the full brunt of

these bending moments directly. This biomechanical difference suggests that implants may face more significant challenges in resisting forces in the transverse plane compared to the sagittal plane during normal locomotion. Therefore, testing in the transverse plane may provide more critical information about an implant's performance under stress. The second impetus for testing in the transverse rather than sagittal plane is that from a surgical perspective, bolts are preferentially inserted from a lateral approach to the femur. Finally, focusing on mediolateral bending, allowed us to assess how well the implant can resist bending forces and maintain proper alignment under conditions that mimic varus and valgus stresses. In contrast, cranio-caudal bending does not directly address these types of forces as it relates more to procurvatum (excessive forward bowing) and recurvatum (excessive backward bending of the bone). Therefore, we opted not to include cranio-caudal bending tests in our study, as they would not have yielded information applicable to the study.

We elected to study 7° of displacement in mediolateral bending tests to simulate realistic varus conditions that usually are present in dogs with femoral varus deformity. Normal physiological femoral varus in dogs is approximately 5° and correction is typically recommended when the DFV exceeds 12° (6,9,11). Seven degrees reflects the difference between these values. As such, if a dog presents with a 12° varus deformity accompanied by medial patellar luxation (MPL), correction is performed to restore a physiological varus of 5° and theoretically this should resolve the condition. Based on this reasoning, it can be speculated that patellar re-luxation might be induced by any correction that is determined to be less than 7°.

The current investigation did not include torsional testing, as the primary objective was to assess the immediate pre-locking stability provided by the I-Loc nail system following DFV correction. The study's focus was on evaluating how well the nail maintained its position and

resisted displacement in the intraoperative period following insertion, but before the locking bolts were secured, rather than examining its strength or resistance to rotational forces prior to and once fully locked into place. Torsional strength, while important in overall implant performance, typically becomes more relevant when considering the nail's ability to withstand twisting forces post-locking, and determining if the effect of compaction makes the nail stronger once it is fully secured/ bone compaction improves its locked strength. Since this study concentrated exclusively on initial immediate stability—a critical factor in preventing early implant failure and promoting proper alignment—torsional testing was deemed clinically irrelevant and beyond the scope of our research goals. Furthermore, compared to plates and/or standard ILNs, the post-locking mechanical superiority of AS-ILN in both torsion and bending has been established in previous studies (28,29).

For the impaction testing, we selected initial stiffness at the 10-20 mm range since this region demonstrated the most linear behavior across all foam densities tested. Additionally, we chose to measure load at 32 mm rather than 35 mm of mandrel advancement to mimic clinical settings where the cancellous tunnel preparation expends beyond the nail’s actual impaction to prevent distraction of the fracture site.

Polyurethane foam has a similar porosity and elastic modulus to cancellous bone (59). It is widely accessible, easy to handle, and enables controlled testing conditions, making it ideal for studies focusing on biomechanics. In our study, we carefully selected different densities of PU foam to simulate various types of canine cancellous bone. Our choices were informed by research in biomechanics and orthopedic implant testing, which have established PU foam as a reliable analog for cancellous bone tissue (59). For low-density canine cancellous bone, we considered 10 PCF foam. This decision was based on previous biomechanical studies that have utilized this foam

density to mimic the mechanical properties of osteoporotic bone (43). Osteoporotic bone is characterized by decreased bone mass and compromised structural integrity, making it an important subject in orthopedic research. We opted to use 12.5 PCF PU foam in our study foam as an appropriate analog model for native cancellous bone. This choice is supported by existing literature in the field (40,60,61). These studies have demonstrated that 12.5 PCF foam exhibits mechanical properties that closely resemble those of natural cancellous bone, making it an excellent substitute for in vitro testing. Additionally, further research has shown that 15 PCF PU foam is often used to simulate normal trabecular or cancellous bone in biomechanical studies (42). This slightly higher density foam represents bone tissue with greater structural integrity compared to the 12.5 PCF variant. To expand our investigation and simulate a wider range of bone conditions, we also incorporated 20 PCF foam into our study. This higher density foam was specifically chosen to represent sclerotic cancellous canine bone. Sclerotic bone is characterized by increased density and hardness, often resulting from various pathological conditions or as a response to mechanical stress. By including this higher density foam, we aimed to model the biomechanical properties of canine cancellous bone that has undergone sclerotic changes. Using synthetic, homogenous test materials allows for greater reliability and reproducibility in our results. Furthermore, bone surrogates help reduce the need for canine specimens, consistent with ethical guidelines that aim to minimize animal use in research.

This study is not without limitations, including the fact that this *in-vitro* experimental system does not fully replicate the inherent complexities of the *in-vivo* condition. Although the polyurethane synthetic bone models provide a consistent and controlled environment for simulating implant site preparation and evaluating the primary stability of the bone-nail interface, clinical application would need to account for additional physiological and biological variables

that could affect patient outcomes. Native canine bone presents density variability and anatomical differences, which could be potential limitations and critical factors when comparing study results to actual clinical conditions. *In-vivo* studies are warranted to determine how this technique may impact the primary stability of the bone-nail interface in cancellous bone.

Future research should focus on including *ex-vivo* or *in-vivo* animal models to validate the findings from this study in clinically relevant settings. This would allow us to evaluate how cancellous bone compaction influences bone healing and remodeling after surgery. *Ex-vivo* models would offer an opportunity to confirm that the effects seen in foam models do translate effectively into dogs with native bones. Long term *in-vivo* models would allow for clinical evaluation of the long-term stability of compacted bone-implant constructs. Over time, natural biological processes such as remodeling could affect the integrity of the compacted bone. Monitoring these processes over a period of weeks or months would provide a clearer picture of whether cancellous compaction maintains its enhanced initial stability or if it leads to complications such as implant loosening, malunion, or nonunion. Additionally, *in-vivo* studies would permit the evaluation of functional outcomes**,** such as limb usage, weight-bearing ability, and overall animal mobility postoperatively. Monitoring how well the animals recover after implantation would also provide insight into the practical effectiveness of cancellous bone compaction in correcting limb deformities.

CONCLUSIONS

In a synthetic distal femoral condyle bone model featuring different densities, cancellous bone compaction enhanced the immediate stability of an I-Loc angle-stable nail. This may virtually eliminate loss of femoral alignment and reduce the risk of postoperative patellar re-luxation. Although this technique has yet to be implemented in clinical cases, we anticipate that improved immediate intra-operative stability of the I-Loc nail will simplify the surgical technique and reduce patient morbidity while decreasing the complication rates. This is expected to be particularly valuable in improving clinical outcomes for patients undergoing DFV correction for the treatment of MPL, an increasingly common and debilitating orthopedic condition in medium- and large-breed dogs.

REFERENCES

1. Roush JK. Canine patellar luxation. *Vet Clin North Am Small Anim Pract*. 1993;23:855–868.

2. DeCamp CE, Johnston SA, Dejardin LM, et al. The Stifle Joint. In: DeCamp CE, Johnston SA, Dejardin LM and Schaefer SL, editors. Brinker, Piermattei and Flo's Handbook of Small Animal Orthopedics and Fracture Repair. 5th ed. Elsevier; 2016. pp. 597–616.

3. Kowaleski MP, Boudrieau RJ, Pozzi A. Stifle joint. In: Johnston SA, Tobias KM, editors. Veterinary Surgery Small Animal. 2nd ed. St Louis: Elsevier Saunders; 2017. pp. 1141–1144.

4. Bound N, Zakai D, Butterworth S, et al. The prevalence of canine patellar luxation in three centres. Clinical features and radiographic evidence of limb deviation. *Vet Comp Orthop Traumatol*. 2009;22:32–37.

5. Towle HA, Griffon DJ, Thomas MW, et al. Pre- and postoperative radiographic and computed tomographic evaluation of dogs with medial patellar luxation. *Vet Surg.* 2005;4:265-272.

6. Roch SP, Gemmill TJ. Treatment of medial patellar luxation by femoral closing wedge ostectomy using a distal femoral plate in four dogs. *J Small Anim Pract.* 2008;49(3):152-158.

7. Gibbons SE, Macias C, Tonzing MA, et al. Patellar luxation in 70 large breed dogs. *J Small Anim Pract*. 2006;47:3–9.

8. Dudley RM, Kowaleski MP, Drost WT, et al. Radiographic and computed tomographic determination of femoral varus and torsion in the dog. *Vet Radiol Ultrasound.* 2006;47(6):546-552.

9. Swiderski JK, Palmer RH. Long-term outcome of distal femoral osteotomy for treatment of combined distal femoral varus and medial patellar luxation: 12 cases (1999–2004). *J Am Vet Med Assoc.* 2007;231:1070–1075.

10. Kowaleski MP. Patellar luxation – preoperative evaluation and surgical planning for femoral corrective osteotomy. 13th Conference of the European Society of Veterinary Orthopaedics and Traumatology. September 7-10, 2006, Munich, Germany. pp 87-90.

11. Tomlinson J, Fox D, Cook JL, et al. Measurement of femoral angles in four dog breeds. *Vet Surg.* 2007;36:593–598.

12. Brower BE, Kowaleski MP, Peruski AM, et al. Distal femoral lateral closing wedge osteotomy as a component of comprehensive treatment of medial patellar luxation and distal femoral varus in dogs. *Vet Comp Orthop Traumatol*. 2017;30:20-27.

13. Dunlap AE, Kim SE, Lewis DD, et al. Outcomes and complications following surgical correction of grade IV medial patellar luxation in dogs: 24 cases (2008–2014). *J Am Vet Med Assoc.* 2016;249:208–213.

14. Peruski AM, Kowaleski MP, Pozzi A. Treatment of medial patellar luxation and distal femoral varus by femoral wedge osteotomy in dogs: 30 Cases (2000–2005). Proceedings of the 2nd World Veterinary Orthopaedic Congress; 2006 February 25-March 4; Keystone, CO, USA. p. 240.

15. Fox DB and Tomlinson JL. Principles of angular limb deformity correction. In: Tobias KM and Johnston SA, editors. Veterinary Surgery: Small Animal, 1st ed., pp. 657–668, Saunders, Elsevier, 2012.

16. Kowaleski MP. Minimally invasive osteosynthesis techniques of the femur. *Vet Clin North Am Small Anim Pract.* 2020;50(1):155-182.

17. Déjardin LM, Guiot LP, von Pfeil DJ. Interlocking nails and minimally invasive osteosynthesis. *Vet Clin North Am Small Anim Pract.* 2012;42(5):935-962.

18. Hulse D, Hyman B. Biomechanics of fracture fixation failure. *Vet Clin North Am Small Anim Pract*. 1991;21(4):647–667.

19. Hulse D, Hyman W, Nori M, et al. Reduction in plate strain by addition of an intramedullary pin. Vet Surg 1997;26(6):451–459.

20. Hulse D, Ferry K, Fawcett A, et al. Effect of intramedullary pin size on reducing bone plate strain. *Vet Comp Orthop Traumatol*. 2000;13(4):185–190.

21. Déjardin LM, Lansdowne JL, Sinnott MT, et al. In vitro mechanical evaluation of torsional loading in simulated canine tibiae for a novel hourglass-shaped interlocking nail with a self-tapping tapered locking design. *Am J Vet Res.* 2006;67(4):678-685.

22. Dueland RT, Berglund L, Vanderby R, et al. Structural properties of interlocking nails, canine femora, and femur-interlocking nail constructs. *Vet Surg.* 1996;25(5):386–396.

23. Muir P, Johnson KA, Markel MD. Area moment of inertia for comparison of implant cross-sectional geometry and bending stiffness. *Vet Comp Orthop Traumatol.* 1995;8:146–152.

24. Roe SC. Biomechanics principles of interlocking nails fixation. 8th Annual American College of Veterinary Surgeons Symposium. Chicago, October 8–11, 1998.

25. Gänsslen A, Gösling T, Hildebrand F, et al. Femoral shaft fractures in adults: treatment options and controversies. *Acta Chir Orthop Traumatol Cech.* 2014;81(2):108-117 .

26. Broos PL, Sermon A. From unstable internal fixation to biological osteosynthesis. A historical overview of operative fracture treatment. *Acta Chir Belg.* 2004;104(4): 396–400.

27. Wheeler JL, Lewis DD, Cross AR, et al. Intramedullary interlocking nail fixation in dogs and cats: clinical applications. *Comp Cont Educ Pract.* 2004;26(7): 531–543.

28. Lansdowne JL, Sinnott MT, Déjardin LM, et al. In vitro mechanical comparison of screwed, bolted, and novel interlocking nail systems to buttress plate fixation in torsion and mediolateral bending. *Vet Surg.* 2007;36(4):368-377.

29. Ting D, Cabassu JB, Guillou RP, et al. In vitro evaluation of the effect of fracture configuration on the mechanical properties of standard and novel interlocking nail systems in bending. *Vet Surg.* 2009;38(7):881–887.

30. Wähnert D, Stolarczyk Y, Hoffmeier KL, et al. The primary stability of angle-stable versus conventional locked intramedullary nails. *Int Orthop.* 2012;36(5):1059-1064.

31. Horn J, Linke B, Höntzsch D, et al. Angle stable interlocking screws improve construct stability of intramedullary nailing of distal tibia fractures: a biomechanical study. *Injury.* 2009;40(7):767-771.

32. Zderic I, Gueorguiev B, Blauth M, et al. Angular stable locking in a novel intramedullary nail improves construct stability in a distal tibia fracture model. *Injury.* 2022;53(3):878-884.

33. Cabassu JB, Villwock M, Guillou RP, et al. *In vivo* biomechanical evaluation of a novel angle-stable interlocking nail design in a canine tibial gap fracture model. Abstract presented at the VOS Conference, 2010, Breckenridge, CO.

34. Fauron AH, Gazzola KM, Perry KL, et al. Clinical application of the I-Loc angle-stable interlocking nail in 100 traumatic fractures of the humerus, femur and tibia. Abstract presented at the VOS Conference, 2018, Snowmass, CO.

35. Dejardin LM. Correction of distal femoral angular deformities associated with patellar luxation using an angle stable interlocking nail. Proceedings of the World Small Animal Veterinary Association Congress, 2016, Cartagena, Colombia.

36. Soballe K, E S Hansen ES, B-Rasmussen H, et al. Tissue ingrowth into titanium and hydroxyapatite-coated implants during stable and unstable mechanical conditions. *J Orthop Res.* 1992;10:285-299.

37. Ryd L, Albrektsson BE, Carlsson L, et al. Roentgen stereophotogrammetric analysis as a predictor of mechanical loosening of knee prostheses. *J Bone Jt Surg (Br).* 1995;77:377-383.

38. Chareancholvanich K, Bourgeault C, Schmidt AH, et al. In vitro stability of cemented and cementless femoral stems with compaction. *Clin Orthop.* 2002;394:290.

39. Kold S, Rahbek O, Toft M, et al. Bone compaction enhances implant fixation in a canine gap model. *J Orthop Res.* 2005;23(4):824-30.

40. Szivek JA, Thomas M, Benjamin JB. Characterization of a synthetic foam as a model for human cancellous bone. *J Appl Biomater.* 1993;4(3):269-272.

41. Silbernagel, JT, Kennedy SC, Johnson AL, et al. Validation of canine cancellous and cortical polyurethane foam bone models. *Vet Comp Orthop Traumatol.* 2002;15:200-204.

42. Goldstein SA. The mechanical properties of trabecular bone: dependence on anatomic location and function. *J Biomech.* 1987;20(11-12):1055-1061.

43. Sommers MB, Fitzpatrick DC, Madey SM, et al. A surrogate long-bone model with osteoporotic material properties for biomechanical testing of fracture implants. *J Biomech.* 2007;40(15):3297-3304.

44. Schneider CA, Rasband WS, Eliceiri KW. NIH Image to ImageJ: 25 years of image analysis. *Nat Methods.* 2012;9(7):671-675

45. Mishra P, Pandey CM, Singh U, et al. Descriptive statistics and normality tests for statistical data. *Ann Card Anaesth.* 2019;22(1):67-72.

46. Déjardin LM, Guillou RP, Ting D, et al. Effect of bending direction on the mechanical behaviour of interlocking nail systems. *Vet Comp Orthop Traumatol.* 2009;22(4):264-269.

47. Huwais, S.; Meyer, EG. A Novel osseous densification approach in implant osteotomy preparation to increase biomechanical primary stability, bone mineral density, and bone-to-implant contact. Int. *J. Oral Maxillofac. Implant.* 2017;32,27–36.

48. Di Stefano DA, Arosio P, Perrotti V, et al. Correlation between implant geometry, bone density, and the insertion torque/depth integral: a study on bovine ribs. *Dent J.* 2019:7;25.

49. Attanasio F, Antonelli A, Brancaccio Y, et al. Primary stability of three different osteotomy techniques in medullary bone: an in vitro study. *Dent J.* 2020;8:21.

50. Bogovic V, Svete A, Bajsic I. Effects of a drill diameter on the temperature rise in a bone during implant site preparation under clinical conditions. Proc Inst Mech Eng H. 2016;230(10):907–917.

51. Falisi G, Severino M, Rastelli C, et al. The effects of surgical preparation techniques and implant macro-geometry on primary stability: an in vitro study. *Med Oral Patol Oral Cir Bucal.* 2017;22(2):e201–e206.

52. Summers RB. A new concept in maxillary implant surgery: the osteotome technique. *Compendium.* 1994;15(2):152-158.

53. Coyac BR, Leahy B, Salvi G, et al. A preclinical model links osseo-densification due to misfit and osseo-destruction due to stress/strain. *Clin. Oral Implant. Res.* 2019;30:1238–1249.

54. Antonelli A, Bennardo F, Brancaccio Y, et al. Can bone compaction improve primary implant stability? An in vitro comparative study with osseodensification technique. *Appl Sci*. 2020;10(23):8623.

55. Jimbo R, Tovar N, Anchieta RB, et al. The combined effects of undersized drilling and implant macrogeometry on bone healing around dental implants: an experimental study. *Int J Oral Maxillofac Surg.* 2014;43(10):1269-1275.

56. Fanali S, Tumedei M, Pignatelli P, et al. Implant primary stability with an osteocondensation drilling protocol in different density polyurethane blocks. *Comput. Methods Biomech. Biomed. Eng.* 2020;25:1–7.

57. Channer MA, Glisson RR, Seaber AV, et al: Use of bone compaction in total knee arthroplasty. *J Arthroplasty*. 1996;11:743–749.

58. Green JR, Nemzek JA, Arnoczky SP, et al: The effect of bone compaction on early fixation of porous-coated implants. *J Arthroplasty.* 1999;14:91–97.

59. Chapman JR, Harrington RM, Lee KM, et al. Factors affecting the pullout strength of cancellous bone screws. *J Biomech Eng.* 1996;118(3):391-398.

60. Thompson MS, McCarthy ID, Lidgren L, Ryd L. Compressive and shear properties of commercially available polyurethane foams. *J Biomech Eng*. 2003;125(5):732-734.

61. Hsu JT, Huang HL, Chang CH, et al. Relationship of three-dimensional bone-to-implant contact to primary implant stability and peri-implant bone strain in immediate loading: microcomputed tomographic and in vitro analyses. *Int J Oral Maxillofac Implants.* 2013;28(2):367-374.

APPENDIX

Table 1: Results of mediolateral bending for 2 groups: drilled (DRILL) and compacted (COMP) foams of all tested densities.

			Stiffness (N/m)			Load (N)	
			Initial (0-5 mm)	Mid (10-15 mm)	Final (14-19 mm)	5 mm	Max
7.5 PCF	**DRILL**	#1	1.28	0.5	-0.54	5.94	16.42
		#2	1.04	0.35	0.98	5.14	16.52
		#3	0.97	0.51	0.41	4.63	16.12
		#4	1.33	0.12	0.07	6.45	16.37
		#5	1.35	0.24	0.11	6.74	16.07
7.5 PCF	**COMP**	#1	1.84	0.06	0.22	9.39	15.59
		#2	1.26	0.62	0.55	6.45	18.43
		#3	1.51	0.32	0.81	7.88	16.6
		#4	1.21	0.27	0.17	6.45	15.29
		#5	1.51	0.01	0.32	8.00	15.58
10 PCF	**DRILL**	#1	1.90	1.31	0.62	9.04	29.27
		#2	2.20	1.32	0.33	10.11	29.92
		#3	2.14	1.31	0.59	9.89	31.65
		#4	2.07	0.39	0.49	9.73	22.81
		#5	2.02	1.29	1.54	9.80	33.43
10 PCF	**COMP**	#1	3.40	0.90	0.67	17.87	32.18
		#2	3.19	1.30	0.09	16.99	32.79
		#3	3.45	1.02	0.32	17.66	31.01
		#4	3.11	0.48	0.19	16.61	26.65
		#5	3.57	0.39	0.56	18.48	27.34
12.5 PCF	**DRILL**	#1	2.64	1.96	1.38	12.72	40.70
		#2	2.60	2.10	1.87	12.16	41.63
		#3	2.38	1.98	1.27	11.60	39.34
		#4	2.46	1.35	1.25	11.78	36.28
		#5	2.59	1.15	1.01	12.06	34.11
12.5 PCF	**COMP**	#1	4.49	1.48	0.61	22.71	43.83
		#2	4.46	1.92	1.81	20.87	52.88
		#3	4.39	1.72	2.14	22.24	52.25
		#4	4.79	1.74	1.94	23.50	52.59
		#5	3.99	0.98	1.79	19.75	41.53

Table 1 (cont'd)

			Stiffness (N/m)			Load (N)	
			Initial (0-5 mm)	Mid (10-15 mm)	Final (14-19 mm)	5 mm	Max
15 PCF	**DRILL**	#1	4.43	3.26	2.22	22.10	70.64
		#2	4.75	2.85	2.29	23.66	72.76
		#3	4.29	3.79	3.34	21.49	78.66
		#4	4.06	3.33	2.35	20.51	72.36
		#5	4.51	2.57	2.16	22.32	69.67
15 PCF	**COMP**	#1	6.96	3.18	2.47	34.06	87.42
		#2	6.51	2.85	2.93	32.89	83.12
		#3	6.81	3.39	2.92	34.11	89.51
		#4	6.60	3.26	2.67	33.04	85.07
		#5	6.49	2.99	2.73	32.18	83.12
20 PCF	**DRILL**	#1	4.43	3.17	4.16	21.66	89.70
		#2	4.43	4.24	2.43	21.14	88.52
		#3	4.43	4.10	3.12	21.12	87.25
		#4	5.03	3.77	2.99	23.04	87.93
		#5	4.08	3.76	2.47	20.29	84.40
20 PCF	**COMP**	#1	6.89	6.16	4.88	34.54	121.00
		#2	6.78	5.37	3.51	35.05	108.81
		#3	6.82	5.02	3.88	35.40	109.28
		#4	6.91	6.00	4.75	35.35	122.49
		#5	7.05	6.41	4.88	35.57	123.31

Table 2: Impaction data with mandrels (4-7 mm) and I-Loc nail across all tested densities.

			Initial stiffness (N/m) (10-20 mm)	Load (N) (32 mm)
7.5 PCF	Mandrel 4	Specimen 1	3.9	80.08
		Specimen 2	5.3	117.89
		Specimen 3	0.9	64.54
		Specimen 4	5.9	113
7.5 PCF	Mandrel 5	Specimen 1	0.9	51.26
		Specimen 2	4.4	72.93
		Specimen 3	2.3	72.00
		Specimen 4	4.6	70.12
7.5 PCF	Mandrel 6	Specimen 1	Not performed	
		Specimen 2		
		Specimen 3		
		Specimen 4		
7.5 PCF	Mandrel 7	Specimen 1	Not performed	
		Specimen 2		
		Specimen 3		
		Specimen 4		
7.5 PCF	Nail	Specimen 1	Not performed	
		Specimen 2		
		Specimen 3		
		Specimen 4		
10 PCF	Mandrel 4	Specimen 1	1.9	97.22
		Specimen 2	1.1	80.56
		Specimen 3	3.5	102.56
		Specimen 4	2.4	85.77
10 PCF	Mandrel 5	Specimen 1	6.3	186.76
		Specimen 2	6.1	146.10
		Specimen 3	7.2	134.64
		Specimen 4	5.3	147.23
10 PCF	Mandrel 6	Specimen 1	7.2	214.78
		Specimen 2	6.6	201.32
		Specimen 3	5.7	216.71
		Specimen 4	7.7	178.71
10 PCF	Mandrel 7	Specimen 1	8.6	238.29
		Specimen 2	7.2	210.05
		Specimen 3	10.1	230.82
		Specimen 4	5.9	250.15
10 PCF	Nail	Specimen 1	7.4	162.81
		Specimen 2	7.7	168.52
		Specimen 3	8.1	200.13
		Specimen 4	6.6	179.92

Table 2 (cont'd)

			Initial stiffness (N/m) (10-20 mm)	Load (N) (32 mm)
12.5 PCF	Mandrel 4	Specimen 1	4.51	116.28
		Specimen 2	6.18	124.08
		Specimen 3	6.38	143.41
		Specimen 4	7.08	151.25
12.5 PCF	Mandrel 5	Specimen 1	8.63	219.44
		Specimen 2	9.21	224.96
		Specimen 3	9.34	268.44
		Specimen 4	10.41	244.46
12.5 PCF	Mandrel 6	Specimen 1	9.14	301.87
		Specimen 2	11.72	332.96
		Specimen 3	10.61	345.88
		Specimen 4	11.8	358.71
12.5 PCF	Mandrel 7	Specimen 1	14.09	378.61
		Specimen 2	12.99	408.62
		Specimen 3	14.92	426.35
		Specimen 4	16.49	428.96
12.5 PCF	Nail	Specimen 1	11.22	311.76
		Specimen 2	12.19	313.62
		Specimen 3	13.56	318.90
		Specimen 4	11.27	320.27
15 PCF	Mandrel 4	Specimen 1	11.2	254.50
		Specimen 2	10.5	285.39
		Specimen 3	12.9	319.59
		Specimen 4	14.7	332.73
15 PCF	Mandrel 5	Specimen 1	16.8	476.59
		Specimen 2	18.0	499.57
		Specimen 3	18.1	512.91
		Specimen 4	16.2	492.05
15 PCF	Mandrel 6	Specimen 1	23.1	636.08
		Specimen 2	23.2	653.02
		Specimen 3	23.9	720.76
		Specimen 4	26.2	726.60
15 PCF	Mandrel 7	Specimen 1	26.4	752.20
		Specimen 2	27.1	792.78
		Specimen 3	28.4	832.50
		Specimen 4	29.5	840.93
15 PCF	Nail	Specimen 1	22.4	595.66
		Specimen 2	23.8	623.00
		Specimen 3	25.3	666.00
		Specimen 4	23.9	660.51

Table 2 (cont'd)

			Initial stiffness (N/m) (10-20 mm)	Load (N) (32 mm)
20 PCF	Mandrel 4	Specimen 1	17.9	394.75
		Specimen 2	31.2	554.73
		Specimen 3	31.4	575.43
		Specimen 4	26.2	574.26
20 PCF	Mandrel 5	Specimen 1	27.6	719.58
		Specimen 2	50.1	1000.40
		Specimen 3	46.1	1057.50
		Specimen 4	48.5	1130.30
20 PCF	Mandrel 6	Specimen 1	40.4	1003.56
		Specimen 2	52.4	1244.70
		Specimen 3	51.5	1496.50
		Specimen 4	61.9	1392.70
20 PCF	Mandrel 7	Specimen 1	41.3	1260.32
		Specimen 2	57.7	1371.10
		Specimen 3	63.7	1595.00
		Specimen 4	79.2	1736.70
20 PCF	Nail	Specimen 1	27.5	825.16
		Specimen 2	45.3	1031.70
		Specimen 3	45.6	1042.40
		Specimen 4	48.8	1110.30

Table 3: Summary of micro-CT data according to foam density (PCF) and preparation technique, drilled (DRILL) and compacted (COMP).

				Total Area, (pixels^2)	Foam Area, (pixels^2)	Area Fraction (%)
7.5 PCF	**DRILL**	Cylinder 1	Hole Area	32052.00	0.00	0.00
			Total Area	229904.00	17343.96	7.54
			Foam Area	197852.00	17343.96	8.77
			Peripheral Area	166572.00	14499.72	**8.70**
			Compacted Area	31280.00	2844.24	**9.09**
		Cylinder 2	Hole Area	32052.00	0.00	0.00
			Total Area	229904.00	19516.55	8.49
			Foam Area	197852.00	19516.55	9.86
			Peripheral Area	166572.00	14902.81	**8.95**
			Compacted Area	31280.00	4613.74	**14.75**
		Cylinder 3	Hole Area	32052.00	0.00	0.00
			Total Area	229904.00	15677.15	6.82
			Foam Area	197852.00	15677.15	7.92
			Peripheral Area	166572.00	11566.91	**6.94**
			Compacted Area	31280.00	4110.25	**13.14**
7.5 PCF	**COMP**	Cylinder 1	Hole Area	28968.00	0.00	0.00
			Total Area	223084.00	16804.92	7.53
			Foam Area	194116.00	16804.92	8.66
			Peripheral Area	159752.00	13960.68	**8.74**
			Compacted Area	34364.00	2844.24	**8.28**
		Cylinder 2	Hole Area	32218.00	6.12	0.02
			Total Area	223084.00	22174.55	9.94
			Foam Area	190866.00	22168.43	11.61
			Peripheral Area	159752.00	17560.81	**10.99**
			Compacted Area	31114.00	4607.61	**14.81**
		Cylinder 3	Hole Area	32218.00	288.03	0.89
			Total Area	223084.00	19841.09	8.89
			Foam Area	190866.00	19553.06	10.24
			Peripheral Area	159752.00	15730.84	**9.85**
			Compacted Area	31114.00	3822.22	**12.28**

Table 3 (cont'd)

				Total Area, (pixels^2)	Foam Area, (pixels^2)	Area Fraction (%)
10 PCF	**DRILL**	Cylinder 1	Hole Area	42628	11.94	0.03
			Total Area	214828.00	29330.47	13.65
			Foam Area	172200.00	29318.53	17.03
			Peripheral Area	148840.00	25991.47	**17.46**
			Compacted Area	23360.00	3327.06	**14.24**
		Cylinder 2	Hole Area	42628.00	135.13	0.32
			Total Area	214828.00	19474.16	9.07
			Foam Area	172200.00	19339.03	11.23
			Peripheral Area	148840.00	17284.02	**11.61**
			Compacted Area	23360.00	2055.01	**8.80**
		Cylinder 3	Hole Area	42628.00	126.18	0.30
			Total Area	214828.00	23048.90	10.73
			Foam Area	172200.00	22922.72	13.31
			Peripheral Area	148840.00	18955.66	**12.74**
			Compacted Area	23360.00	3967.06	**16.98**

10 PCF	**COMP**	Cylinder 1	Hole Area	32988.00	3.96	0.01
			Total Area	218976.00	35905.49	16.40
			Foam Area	185988.00	35901.54	19.30
			Peripheral Area	156188.00	30550.31	**19.56**
			Compacted Area	29800.00	5351.23	**17.96**
		Cylinder 2	Hole Area	32988.00	282.05	0.86
			Total Area	218976.00	38822.26	17.73
			Foam Area	185988.00	38540.21	20.72
			Peripheral Area	156188.00	29167.34	**18.67**
			Compacted Area	29800.00	9372.86	**31.45**
		Cylinder 3	Hole Area	32988.00	46.84	0.14
			Total Area	218976.00	38577.00	17.62
			Foam Area	185988.00	38530.16	20.72
			Peripheral Area	156188.00	29674.92	**19.00**
			Compacted Area	29800.00	8855.24	**29.72**

Table 3 (cont'd)

				Total Area, (pixels^2)	Foam Area, (pixels^2)	Area Fraction (%)
12.5 PCF	**DRILL**	Cylinder 1	Hole Area	39752.00	516.78	0.01
			Total Area	211532.00	59692.22	28.22
			Foam Area	171780	59175.44	34.45
			Peripheral Area	136088.00	49024.43	**36.02**
			Compacted Area	35692.00	10151.01	**28.44**
		Cylinder 2	Hole Area	38704	309.63	0.01
			Total Area	215684	58888.20	27.30
			Foam Area	176980.00	58578.57	33.10
			Peripheral Area	145460.00	49077.21	**33.74**
			Compacted Area	31520.00	9501.36	**30.14**
		Cylinder 3	Hole Area	37632.00	1317.12	0.04
			Total Area	215652.00	59951.26	27.80
			Foam Area	178020.00	58634.14	32.94
			Peripheral Area	146376.00	49710.18	**33.96**
			Compacted Area	31644.00	8923.95	**28.20**

12.5 PCF	**COMP**	Cylinder 1	Hole Area	32988.00	0.00	0.00
			Total Area	217724.00	67760.06	31.12
			Foam Area	184736.00	67760.06	36.68
			Peripheral Area	153028.00	49581.78	**32.40**
			Compacted Area	31708.00	18178.28	**57.33**
		Cylinder 2	Hole Area	32988.00	0.00	0.00
			Total Area	217724.00	69793.61	32.06
			Foam Area	184736.00	69793.61	37.78
			Peripheral Area	153028.00	50635.83	**33.09**
			Compacted Area	31708.00	19157.78	**60.42**
		Cylinder 3	Hole Area	32988.00	0.00	0.00
			Total Area	217724.00	66405.82	30.50
			Foam Area	184736.00	66405.82	35.95
			Peripheral Area	153028	48588.54	**31.75**
			Compacted Area	31708.00	17817.28	**56.19**

Table 3 (cont'd)

				Total Area, (pixels^2)	Foam Area, (pixels^2)	Area Fraction (%)
15 PCF	**DRILL**	Cylinder 1	Hole Area	39415.00	1.18	0.00
			Total Area	216492.00	43016.96	19.87
			Foam Area	177077.00	43015.78	24.29
			Peripheral Area	143920.00	34370.01	**23.88**
			Compacted Area	33157.00	8645.77	**26.08**
		Cylinder 2	Hole Area	39415.00	87.11	0.22
			Total Area	216492.00	46394.24	21.43
			Foam Area	177077.00	46307.13	26.15
			Peripheral Area	143920.00	37758.17	**26.24**
			Compacted Area	33157.00	8548.96	**25.78**
		Cylinder 3	Hole Area	39415.00	0.00	0.00
			Total Area	216492.00	42350.17	19.56
			Foam Area	177077.00	42350.17	23.92
			Peripheral Area	143920.00	34783.81	**24.17**
			Compacted Area	33157.00	7566.36	**22.82**

15 PCF	**COMP**	Cylinder 1	Hole Area	33964	272.05	0.80
			Total Area	225620.00	43375.45	19.23
			Foam Area	191656.00	43101.39	22.49
			Peripheral Area	164460.00	33289.55	**20.24**
			Compacted Area	27196.00	9813.84	**36.09**
		Cylinder 2	Hole Area	33964.00	178.99	0.53
			Total Area	225620.00	45157.84	20.02
			Foam Area	191656.00	44978.85	23.47
			Peripheral Area	164460.00	34930.06	**21.24**
			Compacted Area	27196.00	10048.80	**36.95**
		Cylinder 3	Hole Area	33964.00	229.94	0.68
			Total Area	225620.00	45484.99	20.16
			Foam Area	191656.00	45255.06	23.61
			Peripheral Area	164460.00	34559.98	**21.01**
			Compacted Area	27196.00	10695.07	**39.33**

Table 3 (cont'd)

				Total Area, (pixels^2)	Foam Area, (pixels^2)	Area Fraction (%)
20 PCF	**DRIL**	Cylinder 1	Hole Area	39752.00	516.78	0.01
			Total Area	211532.00	59692.22	28.22
			Foam Area	171780.00	59175.44	34.45
			Peripheral Area	136088.00	49024.43	**36.02**
			Compacted Area	35692.00	10151.01	**28.44**
		Cylinder 2	Hole Area	38704.00	309.63	0.01
			Total Area	215684.00	58888.20	27.30
			Foam Area	176980.00	58578.57	33.10
			Peripheral Area	145460.00	49077.21	**33.74**
			Compacted Area	315200.00	9501.36	**30.14**
		Cylinder 3	Hole Area	37632.00	1317.12	0.04
			Total Area	215652.00	59951.26	27.80
			Foam Area	178020.00	58634.14	32.94
			Peripheral Area	146376.00	49710.18	**33.96**
			Compacted Area	31644.00	8923.95	**28.20**
20 PCF	**COMP**	Cylinder 1	Hole Area	32988.00	0.00	0.00
			Total Area	217724.00	67760.06	31.12
			Foam Area	184736.00	67760.06	36.68
			Peripheral Area	153028.00	49581.78	**32.40**
			Compacted Area	31708.00	18178.28	**57.33**
		Cylinder 2	Hole Area	32988.00	0.00	0.00
			Total Area	217724.00	69793.61	32.06
			Foam Area	184736.00	69793.61	37.78
			Peripheral Area	153028.00	50635.83	**33.09**
			Compacted Area	31708.00	19157.78	**60.42**
		Cylinder 3	Hole Area	32988.00	0.00	0.00
			Total Area	217724.00	66405.82	30.50
			Foam Area	184736.00	66405.82	35.95
			Peripheral Area	153028.00	48588.54	**31.75**
			Compacted Area	31708.00	17817.28	**56.19**